The *Stenotrophomonas maltophilia* MntR miniregulon includes novel extracytoplasmic components and affects replication in *Acanthamoeba castellanii* phagosomes

Fulvia-Stefany Argueta-Zepeda[1,2], Javier Rivera[1], Julio César Valerdi-Negreros[1,3] https://orcid.org/0000-0001-7536-5483, Christopher Rensing[4] https://orcid.org/0000-0002-5012-7953, and Pablo Vinuesa[1] https://orcid.org/0000-0001-6119-2956

[1]Centro de Ciencias Genómicas, Universidad Nacional Autónoma de México (UNAM), Cuernavaca, Morelos, México
[2]Programa de Maestría y Doctorado en Ciencias Bioquímicas, UNAM, Mexico City, Mexico
[3]Programa de Doctorado en Ciencias Biomédicas, UNAM, Mexico City, Mexico
[4]Fujian Agriculture and Forestry University, Fuzhou, China.

Address correspondence to Pablo Vinuesa, vinuesa@ccg.unam.mx

Keywords: AlphaFold, protein structural models, metal-homeostasis, host-microbe interactions, intracellular replication, nutritional immunity

ABSTRACT

Manganese homeostasis is crucial for bacterial survival, particularly in opportunistic pathogens such as *Stenotrophomonas maltophilia,* which switch lifestyles between contrasting environments. This study elucidated the manganese homeostasis system in *S. maltophilia* strain Sm18, a Mexican environmental isolate, revealing a sophisticated network that includes conserved and novel components. We focused on the MntR miniregulon, which comprises the well-known inner membrane importer MntH and exporter MntP, both regulated by the Mn2+-responsive MntR metalloregulator. However, it also contains a TonB-dependent receptor (TBDR) with a distinctive CQNC motif likely involved in Mn2+ coordination and a

periplasmic thioredoxin-fold protein (pTFP). Both are co-expressed from a bicistronic operon under severe manganese and iron limitations and belong to novel families with a limited phyletic distribution. Transcriptomic profiling under varying Mn and Fe concentrations revealed a tight interplay between these metals, emphasizing the ferrophilic nature of *S. maltophilia* and the differential expression of MntR regulon core members. Additional transporters of the RND and CDF families were modulated under dual metal limitation. Mutant analysis demonstrated that MntP is critical for survival, even at Mn levels that do not affect growth kinetics. MntH is required for optimal intracellular replication within *Acanthamoeba castellanii* phagosomes, highlighting its role in overcoming nutritional immunity. Our findings offer new insights into the remarkable adaptability of *S. maltophilia* to diverse environments, contributing to its success as an opportunistic pathogen in humans.

IMPORTANCE

Stenotrophomonas maltophilia is an emerging multidrug-resistant opportunistic pathogen of increasing clinical significance. Understanding the mechanisms of metal homeostasis is crucial for unraveling the physiological adaptability of *S. maltophilia* to diverse niches and its pathogenicity. This study provides the first comprehensive characterization of manganese homeostasis in *S. maltophilia*, revealing novel extracytoplasmic components and their regulatory mechanisms. The identification of a novel TBDR family with a CQNC motif, which is co-transcribed in an operon with a periplasmic pTFP as part of the manganese miniregulon, was unexpected and likely represents a novel post-transcriptional mechanism for TBDR assembly or regulation. Furthermore, demonstrating the importance of MntH in intracellular replication within amoebae provides crucial insights into *the strategies employed by S. maltophilia to* overcome the host's nutritional immunity. These findings contribute to our fundamental knowledge of bacterial physiology and highlight potential targets for developing new therapeutic strategies against *S. maltophilia* and possibly other opportunistic pathogens.

INTRODUCTION

Stenotrophomonas maltophilia is a gram-negative, non-fermentative bacterium recognized for its ecological versatility and opportunistic pathogenicity (1). It thrives in diverse environments, including soil, water, plant rhizospheres, free-living amoebae, and diverse animal organs and cells, demonstrating remarkable adaptability to contrasting ecological niches (2–4). These bacteria can survive harsh conditions, such as oligotrophic or metal-rich environments, and are highly resistant to disinfectants and multiple drugs owing to their robust biofilm formation and multiple efflux systems. Recent research has highlighted these adaptive mechanisms, showing how they enhance the resilience and persistence of *S. maltophilia* in hospital environments (1, 5), making it one of the ten most prevalent microorganisms in hospital care units (6). This pathogen primarily affects immunocompromised individuals, leading to respiratory tract, bloodstream, and urinary tract infections (1), and poses a significant challenge in clinical settings because of its intrinsic resistance to multiple antibiotics, including carbapenems (4, 7). However, little is known about the genes and mechanisms involved in *the adaptation of Stenotrophomonas* to host-associated and intracellular lifestyles in diverse host tissues and phagocytic cells, such as free-living amoebae (3, 8), and mammalian macrophages (9). In recent years, mounting evidence has revealed that professional phagocytes subject phagocytosed bacteria to limiting or toxic concentrations of transition metals, inhibiting their proliferation in phagosomes, a process known as nutritional immunity (10). The homeostasis and balance of essential transition metals, such as manganese, iron, copper, and zinc, are crucial for various physiological processes (11, 12). Metallostasis is controlled by a coordinated network of allosteric metalloregulators, metal transporters, metal-binding proteins, and efflux pumps (13). These components work together to regulate the intracellular metal concentration, ensuring that they are available for essential functions without reaching toxic levels (14). Furthermore, the ability of bacteria to adapt to different environments is closely linked to their metal homeostasis capabilities, which can vary widely across tissues and organs. For instance, the liver is the primary storage site for manganese in the human body, with concentrations of approximately 10 μM (15). Similar levels are observed in mouse organs (16). In contrast, serum manganese levels are kept low, typically less than 10 nM (17). Moreover, the modulation of iron (Fe) and manganese (Mn) levels, along with other trace elements, in different tissues during bacterial infections in mice highlights the critical role of metal homeostasis in the establishment and progression of infections (16, 18).

Studies on *S. maltophilia* metallostasis have focused on iron homeostasis, highlighting its importance in bacterial virulence (19). In contrast, our knowledge of the molecular mechanisms underlying manganese homeostasis in *Stenotrophomonas* is limited to a single transcriptomic study performed on *Stenotrophomonas* sp. MNB17, an organism isolated from a deep-sea mud sample in the western Pacific, removes Mn^{2+} by efficiently forming Mn-precipitates ($MnCO_3$ and Mn oxides) at high Mn concentrations (20). However, manganese homeostasis has been well studied in some Gram-positive and Gram-negative bacteria (21, 22). In these organisms, a crucial component of manganese homeostasis is the inner membrane manganese transporter protein MntH, which facilitates manganese uptake from the periplasm into the cytoplasm under limiting conditions (23). Conversely, the inner membrane exporter protein MntP removes excess manganese, thereby maintaining intracellular levels within the optimal range (24). This process is regulated by various regulatory proteins and signaling pathways that sense intracellular manganese levels and adjust the expression or activity of manganese transporters (25, 21, 26), with MntR being the most studied (24, 27). Furthermore, under manganese limitation and oxidative stress, an Mn^{2+}-scavenging pathway has been identified in *Burkholderia thailandensis*, comprising a newly discovered TonB-dependent outer membrane (OM) manganese transporter, MnoT, and an Mn^{2+}-binding protein, TseM, secreted by a type VI secretion pathway (T6SS) (28), which is apparently unique to Burkholderia species (10).

The requirement for Mn^{2+} and Fe^{2+} varies greatly among bacterial species (21). *S. maltophilia* features an iron-centric metabolism that requires iron for optimal growth and virulence (19, 29). However, Mn^{2+} becomes essential under oxidative stress or low iron availability (30), conditions that mirror the environments that *S. maltophilia* likely encounters as an intracellular opportunistic pathogen in phagosomes subjected to nutritional immunity (10, 31). This bacterium has been reported to survive in human epidermoid epithelial cells (32), human lung epithelial cells (33, 34), free-living amoebae (3, 8), and mammalian macrophages (9, 33). The divalent Mn^{2+}/Fe^{2+} transporter Nramp1 protein, located in the phagosomal membrane and ubiquitous in eukaryotes, plays a crucial role in nutritional immunity by depleting phagocytosed bacteria of these micronutrients. Interestingly, its bacterial homolog, MntH, is also essential for countering this stress by importing Mn^{2+} into bacterial cells (35, 36).

Here, we present a detailed genomic, evolutionary, and functional analysis of *Stenotrophomonas* manganese homeostasis systems, demonstrating their contribution to

bacterial fitness in *Acanthamoeba castellanii* phagosomes for the first time. We identified the key components of the MntR miniregulon in *S. maltophilia* Sm18, a Mexican environmental isolate (4, 37), and subjected them to genetic and functional analyses. We demonstrated that the Sm18Δ*mntP* deletion strain was susceptible to Mn^{2+} *in vitro*. We identified two new genes of the miniregulon organized in an operon encoding a TonB-dependent receptor (TBDR) containing a conserved CQNC motif and a periplasmic thioredoxin-fold protein (pTFP), which have not been previously reported in other bacteria to be manganese-regulated. Phylogenomic and comparative genomic analyses revealed that both proteins belong to novel families. Detailed studies of AlphaFold structural models have revealed key features of likely functional relevance. RNA-Seq-based transcriptome analyses performed under limiting iron and manganese concentrations revealed that the TBDR-pTFP locus and *mntH* gene are derepressed, underscoring their importance in maintaining metal homeostasis in metal-restricted environments such as the phagosomes of diverse phagocytes. We recently reported that Sm18 can survive and replicate in the acidified Rab7A-positive vacuoles of *Acanthamoeba castellanii* trophozoites (3). Here, we report that the *mntH* gene is expressed and required for optimal intracellular replication in the phagosomes of this free-living professional phagocyte.

RESULTS

Complete genome sequencing and annotation of *Stenotrophomonas maltophilia* ESTM1D_MKCAZ16_6a (Sm18). All experiments in this study were performed using *S. maltophilia* ESTM1D_MKCAZ16_6a (Sm18), a multidrug-resistant strain recovered from the sediments of a clean river in Morelos, Central Mexico (4). A full description of the complete genome sequence is provided in a companion paper (37). The Sm18 genome assembly was derived from short paired-end Illumina MiSeq (2 × 300 bp) reads and long MinION (Oxford Nanopore Technologies) reads and consisted of a single circular chromosome of 4,482,207 bp. Gene calling and genome annotation were performed using the NCBI PGAP pipeline (38), identifying 3,970 CDSs encoding proteins and 24 pseudogenes. GenBank's genome sequence and annotation are available under accession number CP146374, with associated BioProject and BioSample identifiers PRJNA1081934 and SAMN40194962, respectively. Average blast nucleotide identity (ANIb) analyses computed with GET_PHYLOMARKERS

(39) and reported in (37) confirmed that Sm18 is a *bona fide S. maltophilia* strain, as previously determined by multilocus sequence analysis and population genetics (4).

Manganese impact on *S. maltophilia* Sm18 growth kinetics in complex and defined media The first step in characterizing the manganese homeostasis system of Sm18 was to assess the strain's manganese tolerance. We ran 48-hour growth kinetics using complex Luria-Bertani (LB) and minimal MOPS (MM) media with increasing $MnCl_2$ concentrations. FIG 1A shows that Sm18 grew in LB and MM up to 16 mM and 8 mM of $MnCl_2$, respectively. In both media, the maximal growth rate and total yield of the culture remained unaffected, except at the highest concentrations at which Sm18 could grow in each medium. However, statistical analysis of the area under the curve (AUC) for population density (OD_{600}) data presented in FIG 1B revealed a significant decrease in growth in both media starting at 8 mM $MnCl_2$, mainly due to the extended lag phase of each growth curve observed with increasing manganese concentration. These results indicate that Sm18 exhibits notably higher tolerance to manganese than other gram-negative bacteria, such as *Escherichia coli* (40).

Genome-wide identification of manganese-responsive genes in *S. maltophilia* Sm18 by RNA-seq analysis under varying manganese and iron concentrations Given our interest in identifying Sm18 genes required for intracellular replication in *Acanthamoeba* phagosomes, a compartment that we hypothesize might limit both Mn^{2+} and iron Fe^{2+} availability to the containing bacteria, we analyzed the transcriptional profile of Sm18 under varying concentrations of both transition metals using RNA-sequencing (RNA-Seq).

The experiments and downstream analyses were conducted using three biological replicates of *Sm18* cultures grown in defined MM medium supplemented with casamino acids, under four contrasting combinations of Fe^{2+} and Mn^{2+} in micromolar (µM) concentrations: (i) Fe0 Mn0, (ii) Fe0 Mn8, (iii) Fe10 Mn0, and (iv) Fe10 Mn8. Principal component analysis (PCA) shown in FIG 2A demonstrated that replicates within each group were clustered and separated according to metal concentration. PC1 revealed that 64% of the variance was related to varying iron conditions, while PC2 explained 10% of the variance due to manganese concentrations. Consequently, we anticipate more differentially expressed genes (DEGs) in response to changes in iron compared to manganese, supporting the classification

of Sm18 as a bacterium with iron-centric metabolism. To validate this hypothesis, we conducted differential gene expression analysis using DESeq2. We identified a total of 124 differentially expressed genes (DEG) when comparing Fe^{2+} 10 μM vs. Fe^{2+} 0 μM in MM-Mn0, and 89 DEGs in MM-Mn8, based on an adjusted P-value (padj) < 0.01 and a $\log_2$ fold change $|(\log_2 FC)| \geq 1.0$ (see Methods). In contrast, only five DEGs were detected when comparing Mn^{2+} 0 μM vs. Mn^{2+} 8 μM in MM-Fe10, and 16 DEG in MM-Fe0. To gain deeper insights into the transcriptional regulation interplay between manganese and iron homeostasis systems in Sm18, we visualized the number of DEGs for each condition as a Venn diagram (FIG 2B). This diagram displays four interconnected ovals, each representing the number of DEGs under the specific conditions mentioned above, illustrating overlaps to identify shared DEGs across conditions. Our analysis revealed that 88 DEGs were regulated solely by iron levels, irrespective of manganese concentrations in the medium. A detailed analysis of these genes will be presented elsewhere (Argueta-Zepeda and Vinuesa, *in preparation*). Among the elements of the manganese miniregulon in Sm18, *mntP* is the only gene exclusively regulated by manganese concentrations in the medium, independent of iron levels (FIG 2B). In contrast, the expression of *mntH* was affected by any change in manganese or iron concentration in the medium (FIG 2B). The latter result aligns with previous reports that *mntH* transcription is regulated by MntR and Fur (21). Nine genes displayed differential expression only when cultures were subjected to simultaneous Fe^{2+} and Mn^{2+} limitation, with their locus tags listed in FIG 2B. Two were downregulated (blue-colored locus tags) under these conditions, whereas the remaining genes were upregulated, as detailed below. Figure 2C highlights the DEG identified when comparing Mn^{2+} 0 μM vs. Mn^{2+} 8 μM in both MM-Fe10 and MM-Fe0 media (see Supplementary Data, Tables 1 and 2 for more details). These DEGs are represented as colored dots on the $\log_2$FC plots, and their corresponding genomic loci are indicated by green vertical bars mapped to the Sm18 chromosome. The molecular gene ontologies (GOs) of the DEGs are highlighted in different colors on the $\log_2$ FC charts, with the transmembrane transport category (yellow points) being the most prevalent. FIG 2C also shows bar charts for the $\log_2$ FC values for the same loci and treatments for a better quantitative representation, including the protein annotations of each DEG. FIG 2C revealed that V8P27_002357, V8P27_002358, and V8P27_004008, encoding a TonB-dependent receptor (TBDR), a periplasmic thioredoxin-fold protein (pTFP), and the well-known cytoplasmic membrane Mn exporter MntP, respectively, are the three genes showing the most significant $\log_2$ FC values, exceeding 2.8 units in absolute values. TBDR and pTFP are circled and, with a few others

mentioned below, are likely involved in the Sm18 transition metal homeostasis system under simultaneous manganese and iron limitation.These proteins were subjected to additional bioinformatic, genetic, and functional characterization, as detailed in the following sections. Finally, in MM supplemented with 8 μM Mn^{2+}, *mntH* expression was repressed, whereas *mntP* showed a >3 Log_2FC increase, presumably to export excess cytoplasmic manganese. Furthermore, in the absence of iron supplementation, other genes were upregulated along with *mntP*, including two predicted transporter proteins, the annotations of which are shown in FIG 2C. In contrast, five genes primarily associated with transmembrane transport were downregulated together with *mntH*, V8P27_002357, and V8P27_002358 (FIG 2C).

Genome-wide scanning for potential MntR binding sites identified the core components of the MntR mini regulon in *S. maltophilia* Sm18. Several Mn^{2+}-responsive genes are known to be regulated by the MntR protein, the master allosteric manganese transport metalloregulator of the DtxR family (41), which recognizes a short inverted palindromic sequence in the 5' UTR region of target loci known as the MntR-box. We performed iterative MEME-MAST (42) searches (see Methods) to identify potential MntR-boxes in a collection of 103 *Lysobacteraceae* genomes described in the following section, resulting in the MEME profile shown in FIG 3A. MAST-based (42) genome-wide scanning of the Sm18 assembly with the MntR-box profile revealed the presence of two additional MntR motifs, defining two additional genomic loci potentially under MntR regulation. The first site was located 75 bp upstream of V8P27_002357, which encodes a putative TonB-dependent receptor (TBDR) closely linked to the *mntR* (V8P27_002359) and *mntH* (V8P27_002360) genes. These genes share a bidirectional promoter, with the MntR-box positioned 10 bp upstream of the *mntH* start codon (FIG 3B), which was shown by RNA-seq to be the DEG with the highest log_2FC value of those displaying differential regulation specifically under both Mn^{2+} and Fe^{2+} limitation (FIGS 2B and 2C). The second site maps 247 bp upstream of *mntP* (V8P27_004008), encoding the key cytoplasmic membrane Mn^{2+} exporter MntP, which is differentially expressed in media with high Mn^{2+} concentrations, irrespective of Fe^{2+} concentration. Similar to *E. coli*, *mntP* in Sm18 is preceded by a putative *yybP-ykoY-like* riboswitch (FIG 3C). Based on this evidence, we postulated that *mntH* and ORFs 2357 and 2358 in the first genomic locus (FIG 3B) and *mntP* (FIG 3C) form the core of a putative MntR miniregulon in *S. maltophilia* Sm18, similar to that defined by Waters et al.

(24) for *Escherichia coli*. Interestingly, the V8P27_002357 gene and the immediately downstream-located putative periplasmic thioredoxin-fold protein (V8P27_002358, pTFP), which is co-transcribed with the preceding TBDR, are not found in MntR regulons reported in other bacteria (43).

Phylogenomic analysis revealed a lineage-specific distribution of MntR miniregulon core members across selected *Lysobacteraceae.*

We used hmmsearch from the HMMER3 suite (44) with calibrated profile hidden Markov models (see methods) to identify MntR*,* MntH, MntP, ORF2357, and ORF2358 homologs across a collection of 103 RefSeq genomes representative of the currently described taxonomic diversity of *Stenotrophomonas* and related genera in the *Lysobacteraceae* (45). Genome-wide MAST scans using the MntR-box profile described in the previous section (FIG 3A) identified 0 to 4 MntR-boxes per genome at a cutoff P-value ≤ $5e^{-8}$, suggesting that not all genomes contain the MntR miniregulon. To study the phylogenetic distribution of its members, we estimated a maximum likelihood species tree for the 103 genomes based on the concatenated supermatrix of 155 top-scoring core genome proteins selected with GET_PHYLOMARKERS (39) out of 601 input core gene families computed with GET_HOMOLOGUES (46). The resulting tree was used to map taxonomic information (39, 45) and integrate it with the presence-absence patterns of hmmsearch hits and the count data of MAST hits for the MntR motif (FIG 4). Only *Stenotrophomonas* species, including *S. maltophilia*, encode these five proteins, which correlates with the presence of three MntR boxes. However, *S. pavanii*, *S. beteli*, and *S. hibiscicola* lack V8P27_002357 (TBDR) and V8P27_002358 (pTFP) proteins and contain only two MntR boxes each. V8P27_002357 and V8P27_002358 homologs were not detected in the *Allostenotrophomonas*, *Pseudostenotrophomonas*, and *Parastenotrophomonas* proteomes. Only the MntP exporter was conserved across the four genera analyzed (FIG 4). In conclusion, within the analyzed *Lyosobacteraceae,* the complete, five-member MntR miniregulon was found to be restricted to the genus *Stenotrophomonas sensu* Chauviat et al. (45).

The expression of *S. maltophilia* Sm18 MntR regulon core genes is modulated by iron and manganese concentrations. To validate the bioinformatic predictions supporting the existence of an MntR miniregulon in *S. maltophilia* complex genomes (FIGS 3 and 4), we

constructed transcriptional fusions of the 5'-UTRs of each of the three core loci of Sm18 to the Green Fluorescent Protein (GFP) using the broad-host-range plasmid pSEVA327 (Sm18/327-2357_2358, Sm18/327-*mntH*, and Sm18/327-*mntP;* supplementary data, Table S4). FIG 5A presents the corresponding promoter activities measured over 40 h as the area under the curve (AUC) of GFP relative fluorescence units (RFU), normalized to the population density (OD_{600}), in response to varying manganese and iron concentrations. Expression data for the Sm18/327-2357_2358 fusion (FIG 5A, first panel) revealed that the operon encoding the novel TonB-dependent receptor and thioredoxin-fold protein was expressed solely under Mn and Fe limitation (Mn^{2+} 0 μM and Fe^{2+} 0 μM), confirming the RNA-seq data (FIG 2). It should be noted that MM contains trace amounts of iron (~1.6 ppm) from the casamino acid (CAA) supplement. However, no GFP signal was detected in MM containing Mn^{2+} 80 nM, either with 0 or 10 μM Fe^{2+}, indicating that this low Mn^{2+} concentration is sufficient to repress expression. The expression profile of the Sm18/327-*mntH* fusion (FIG 5A, second panel) was characterized by a highly significant decline in activity that was negatively correlated with increasing Mn^{2+} concentrations in the culture medium. However, low activity was still measurable at 8 μM Mn^{2+}. A significantly higher activity in the Sm18/327-*mntH* expression profile was observed at Fe^{2+} 10 μM vs. 0 μM, except when the medium contained 8 μM Mn^{2+}. These results again reveal a strong relationship in Sm18 between manganese and iron homeostasis, specifically in manganese uptake systems. This confirms our RNA-seq data and is consistent with observations made in *E. coli* (47, 48). As expected, the expression profile of Sm18/327-*mntP* increased significantly in Mn^{2+} 8 μM, compared to Mn^{2+} 0μM, irrespective of whether the medium was depleted or supplemented with iron (FIG 5A, third panel), in line with the RNA-seq results. As shown in FIG 1, although the upper Mn^{2+} concentration (8 μM) used for these experiments is orders of magnitude below the threshold tolerated by Sm18, it is sufficiently high to induce the cells to down-regulate the expression of importers and activate the MntP exporter to keep intracellular Mn homeostasis. In conclusion, these experimental data validated our RNA-seq results and bioinformatically derived hypotheses regarding the presence of MntR boxes upstream of the core components of the *S. maltophilia* Mn homeostasis system.

The MntR metalloregulator controls the expression of the core components of the Sm18 Mn homeostasis system. To confirm that the promoter activity observed in the transcriptional fusions reported in FIG 5A (previous section) is regulated by MntR, as

suggested by the presence of potential MntR-boxes uncovered by our bioinformatic analysis (FIGS 3 and 4), the three fusions were transferred into an Sm18Δ*mntR* strain carrying a markerless *mntR* deletion (Supplementary Data, Table 3). Promoter activity in iron-deficient MM with manganese concentrations of 0 μM and 8 μM was measured as described in the previous section (FIG 5A). The Sm18ΔmntR/327-2357_2358 fusion (FIG 5B, first panel) revealed a significant increase in expression in the absence of supplemented manganese, suggesting derepression in the absence of the MntR transcription factor. However, adding manganese led to reduced expression, following a similar trend to that observed in the Sm18 wild-type background, suggesting that manganese may negatively regulate this operon via an alternative MntR-independent mechanism. Similarly, derepression of the 327-*mntH* fusion was observed in the Sm18Δ*mntR* genetic background compared to the wild-type growing in MM without supplemented manganese (FIG 5B, second panel). However, no statistically significant activity was detected in the Sm18ΔmntR/327-*mntH* fusion upon adding 8 μM Mn. This suggests that manganese-dependent regulation of *mntH* promoter activity is mediated exclusively by MntR. Finally, the *mntP* fusion exhibited manganese-dependent regulation exclusively through MntR, as no expression was detected in the absence of MntR, independent of manganese concentration, in line with the RNA-seq data (FIG 2).

In conclusion, RNA-seq, bioinformatic, and transcriptional fusion analyses jointly and consistently confirmed that MntR controls the expression of the three core components of the *S. maltophilia* Sm18 MntR miniregulon involved in manganese homeostasis. The *mntH* and *mntP* genes are highly conserved across Gram-negative and Gram-positive bacteria. In contrast, the bicistronic operon formed by V8P27_002357 (TonB-dependent receptor) and V8P27_002358 (thioredoxin-fold protein) represents a novel member of the MntR miniregulon that has not been previously reported in other bacteria.

The V8P27_002357 TonB-dependent receptor belongs to a novel family with a restricted phylogenetic distribution and is characterized by a conserved CQNC motif in its plug domain, which is **likely involved in metal coordination.**

After confirming that V8P27_002357 (TBDR) and V8P27_002358 (pTFP) are members of the MntR miniregulon of *S. maltophilia sensu lato* strains (FIGS 3 and 4) and are subjected to Mn^{2+} regulation (FIGS 2 and 5), we performed a detailed structural and phylogenomic

characterization of these novel proteins to uncover structural features of potential functional significance and gain deeper insights into their potential function, evolution, and phylogenetic distribution. FIG 6 summarizes the findings for V8P27_002357. It encodes a 719 aa TonB-dependent receptor with a 28 bp-long N-terminal signal peptide, resulting in a mature protein of 76.6 kDa (691 aa) containing an N-terminal plug or core domain (141 aa, 15 kDa) featuring a centrally located CQNC motif, followed by a TBDR β-barrel domain (550 aa, 61.6 kDa), as depicted in FIG 6A. We employed AlphaFold3 (AF3) (49) to uncover the features of potential functional relevance from the modeled structure. A high-quality model was obtained (pTM = 0.93 and mean pLDDT = 88.4). FIG 6C shows a side view of the best-scoring model of the mature apo protein, with three structural features of likely functional relevance highlighted in different colors (see figure legend): the TonB box (FIG 6B), CQNC motif (FIG 6D), and one of the salt bridges, which might control substrate passage across the TBDR (FIG 6E). The CQNC motif is located at the tip of a prominent antiparallel β-hairpin protruding toward the extracellular space from the plug domain (FIG 6D). The two cysteine thiol (sulfhydryl) side chains are close to each other (~3.1 Å; PAE = 1.54 Å (Predicted Alignment Error); FIG 6D inset), with the potential to form a disulfide bond in the oxidizing periplasmic environment during the protein's transit to the outer membrane. The plug's N-terminal segment is disorganized and contains a potential TonB box motif (RVQVKV), predicted by the model to be hidden within the β-barrel (FIG 6C). This motif was identified by AF3 modeling (FIG 6B) of the complex formed by the 24 N-terminal residues of V8P27_002357 with the 80 C-terminal amino acids of the Sm18 TonB protein (V8P27_003890) forming its C-terminal domain (CTD), which revealed that RVQVKV formed a parallel β-sheet with residues 71-76 of TonB's CTD (mean PAE 4.18 ± 0.38 Å). Furthermore, residue Arg19 following the Ton box forms a potential salt bridge with D332 located at ~2.5 Å (PAE = 2.07 Å) on the eighth β-strand (FIGS 6C, 6E), potentially forming an ionic lock (IL) that retains the Ton box within the β-barrel, as reported for BTUB_ECOLI, an *E. coli* vitamin B12 TBDR (50, 51). The β-barrel domain displays the canonical structure of 22 antiparallel β-strands with short turns connecting strands on the periplasmic side and large loops and secondary structures oriented toward the extracellular space (FIG 6C).

Given that the expression of the V8P27_002357-V8P27_002358 locus is repressed by as little as 0.08 μM Mn^{2+} (FIG 5A), we also modeled the V8P27_002357 holoprotein with Mn^{2+} (FIG 6F). The AF3 model predicted with high certainty (ipTM = 0.84; pTM =0.90; mean

pLDDT = 87.08) that the cysteines from the CQNC motif were involved in cation binding (FIGS 6F and 6G). To identify the coordinating donor atoms for Mn^{2+}, we searched for residues containing side-chain atoms within 3.5 Å of the cation. This analysis revealed that the metal could be coordinated by two sulfur, one nitrogen, and one oxygen atom arranged in a tetrahedral geometry (FIG 6H), contributed by residues C63, C66, E247, and H446 (FIG 6G), respectively, the latter two located on the β-barrel domain (FIG 6F). To challenge this hypothesis, we measured the distances between the donor atoms and the metal (FIG 6H) and compared them with those reported in the MESPEUS database of coordination groups in proteins (52), focusing on high-resolution structures (≤ 1.8 Å). FIG 6I presents the distribution of the distances (as boxplots) between Mn^{2+} and the coordination donor atoms in Cys (median = 2.3245 ± 0.0259 median absolute deviation, n = 8), Glu (2.08 ± 0.1572, n = 53), and His (2.183 ± 0.2165, n = 66) residues extracted from the MESPEUS database as of March 2025, revealing that the measured coordination bond distances in V8P27_002357 (FIG 6H) are within the expected range, as computed from crystallography data, and very close to their median distances. Taken together, the high AF3 ipTM score, metal-donor distance measurements, and coordination geometry strongly suggest that residues C63, C66, E247, and H446 are directly involved in metal coordination.

Interestingly, the AF3 model for the holoprotein with bound Mn^{2+} predicted an allosteric conformational switch, increasing the distance between the R19 and D332 residues (4.5 Å; PAE = 2.5; FIG 6 J). This would release the IL, allowing the N-terminal sequence and TonB box to protrude from the β-barrel into the periplasmic space (FIGS 6F and 6 J), presumably allowing contact with the TonB CTD. These findings are consistent with the current mechanistic models of TonB transporters (51).

We used BlastP to search for V8P27_002357 homologs (excluding *Stenotrophomonas* hits) in the PDB, Swiss-Prot, and RefSeq protein databases. This analysis revealed a restricted and sparse phylogenetic distribution of the closest hits, which belonged to a few genera in the classes Bacteroidia, Flavobacteriia, Holophagae, Opitutia, Alphaproteobacteria, and Gammaproteobacteria. These sequences and the best hits found in PDB and Swiss-Prot were collected to generate a structure-guided multiple-sequence alignment and estimate a maximum likelihood phylogeny (see Methods section). FIG 6 K depicts a small summary tree, revealing that the closest V8P27_002357 homologs form a perfectly supported (100% bootstrap support) and tightly clustered lineage of sequences, all of which share the distinct

CQNC motif in their plug domain (FIG 6 L). Based on this structural and phylogenetic evidence, we propose that V8P27_002357-like proteins comprise a new CQNC family of TBDRs (FIG 6 K).

V8P27_002358 belongs to a novel family of periplasmic thioredoxin-fold proteins (pTFPs) linked to CQNC-type TBDRs by synteny and co-expression, featuring the WC[AG]PC motif.

The presence of a periplasmic thioredoxin-fold protein (pTFP; matching IPR013766) co-expressed with a preceding CQNC-type TBDR (V8P27_002357 in Sm18) has not been previously reported and suggests that both proteins might be functionally related. To challenge this hypothesis, we performed phylogenomic and comparative genomic analyses of this locus. BLAST searching for V8P27_002358 homologs was performed as described in the previous section for the V8P27_002357 TBDR, but extending the databases with the recently reported metagenomic dataset of thioredoxin superfamily proteins compiled by Nilewski et al. (53). The final dataset contained 203 proteins after removing nearly identical sequences by clustering at 99% sequence identity with CD-HIT. A structure-guided multiple-sequence alignment was computed using mafft-dash, and a maximum likelihood phylogeny was estimated using IQTree. The resulting tree revealed that V8P27_002358 clustered in a highly supported and distinct clade (FIG S1) with uncharacterized sequences from a few genera belonging to the orders Lysobacterales (Gammaproteobacteria), Sphingomonadales (Alphaproteobacteria), and Opitutales (Verrucomicrobiota; Opitutia). We extracted pTFP homologs and flanking genes from the corresponding genome sequences of representative hits for synteny analysis. The V8P27_002358 clade members were located immediately downstream of the CQNC-type TBDR (FIG 7A), strongly reinforcing the notion that they are functionally related. However, the genes flanking the TBDR-pTFP locus were variable (FIG 7A).

V8P27_002358 is 173 aa long and features an N-terminal signal peptide of 23 aa (FIG 1B). The mature protein contained 159 aa, with a computed mass of 17.64 kDa and a periplasmic location, as predicted by Phobius (p = 0.94) and Psortb (score = 9.84). All pTFPs share a minimal thioredoxin fold (TRX-fold) characterized by an N-terminal βαβ fold separated by an α-helix from the C-terminal ββα fold (54). The highly diversified and ubiquitous superfamily of

pTFPs (53, 55, 56) encodes thiol:disulfide oxidoreductases (TDORs) that contain additional secondary structural elements and loops inserted between the conserved domains of the TRX fold. Figure 7B shows the best-scoring AF3 model (pTM = 0.93; mean pLDDT = 92.35) computed for V8P27_002358. The conserved TRX-fold elements are color-coded (see the figure legend). FIG 7B also displays the highly conserved CXXC (C39, C42) motif of thioredoxins and thioredoxin-like proteins found at the beginning of the α1 helix of the TRX fold. The AF3 model for V8P27_002358, shown in FIG 7B, presents the oxidized version of the CXXC motif (disulfide bridge in dark red). The protein contains an additional pair of cysteines at its C-terminus (C147, C154), which is also predicted to form a disulfide bond, as shown in FIG 7B. FIG 7C presents a 2D topological cartoon of the mature V8P27_002358 protein, highlighting the TRX-fold elements and the position of the short extra N-terminal α-helix (Eα1) and β-strands (Eβ1 and Eβ2), and the two extra C-terminal α-helices (Eα2 and Eα3). It is well established that the dipeptide flanked by cysteines in the CXXC motif (57) and other neighboring residues constitute an extended active-site motif controlling the reactivity of TDORs (58). V8P27_002358 contains an unusual CAPC dipeptide in the catalytic CXXC redox center. To gain further functionally relevant structural insights into the novel pTFPs associated with CQNC-type TBDRs (FIG 7A), we performed motif analysis around the β1-α1 region of the TRX-fold, including well-characterized pTFPs (SwissProt codes) with contrasting reduction potentials and pK_a values previously analyzed by Mavridou et al. (58). As shown in FIG 7D, there was considerable diversity in and around the CXXC motif dipeptide. The pTFPs associated with CQNC-type TBDRs are characterized by a distinctive and lineage-specific Y[FYC]GA[DS]WC[AG]PCH[AE]F[VL]P profile overlapping the CXXC motif, derived from the sequence logo shown in FIG 7D. A detailed inspection of the AF3 model around the CXXC motif of V8P27_002358 revealed that residues Y33 and A36, which are strictly conserved in the novel pTFP family (FIG 7E), can establish hydrogen bonds with C39 and C42, potentially affecting their pK_a values and reactivity.

Mutants of MntR miniregulon members result in hydrogen peroxide and manganese sensitivity. To investigate whether the Sm18 *mntH* and *mntP* homologs encode functional manganese importer and exporter proteins, we constructed the interrupted mutant Sm18VIM*mntH* and the markerless deletion mutant Sm18Δ*mntP* (see Methods). The growth kinetics of the Sm18VIM*mntH* mutant indicated that the *mntH* gene is not essential under Fe^{2+}- or Mn^{2+}-limiting conditions in axenic cultures. However, it is required for growth under

oxidative stress induced by hydrogen peroxide (H_2O_2), particularly at neutral pH (FIG 8A). Statistical analysis revealed that the difference in growth was significant only at 500 µM H_2O_2 (FIG 8B). These results are consistent with those of previous studies on bacteria, which demonstrated that *mntH* mutants are sensitive to H_2O_2, a phenotype largely attributed to their impaired ability to import manganese into the intracellular space (30). Conversely, it has been well established in diverse bacterial models that manganese exporter proteins are required to counter manganese toxicity (22, 40). Sm18Δ*mntP* was challenged with increasing concentrations of Mn^{2+} (5 -160 µM; FIG 8C) and exhibited statistically significant sensitivity to manganese beginning at 40 µM, with complete growth inhibition observed at 160 µM (FIG 8D). The wild-type phenotypes of the Sm18VIM-*mntH* and Sm18Δ*mntP* strains were restored by the plasmid pSEVA332 (Sm18VIM-*mntH*/332::*mntH* and Sm18Δ*mntP*/332::*mntP*), provided in trans and carrying the *mntH* and *mntP* genes under the control of their native promoters (FIG 8). These results demonstrate that *mntH* and *mntP* expression is essential for H_2O_2 resistance and manganese detoxification, respectively, and confirm that the uncovered MntR miniregulon is functional. Notably, the markerless mutants of genes V8P27_002357 and V8P27_002358 exhibited no phenotypes under the tested conditions.

The *mntH gene of S. maltophilia* is expressed in *Acanthamoeba castellanii* phagosomes and is required for optimal intracellular replication. We recently found that *S. maltophilia* Sm18 resists digestion by *Acanthamoeba castellanii* strain Neff trophozoites and can replicate in acidified, Rab7A-positive *Stenotrophomonas*-containing vacuoles (SCV) of this free-living professional phagocyte (3). Given that the phagosomes of *Dictyostelium discoideum* and human macrophages subject bacteria to iron and manganese limitation via the NRAMP exporter (59, 60), we postulated that the Sm18 MntH Mn importer is required to survive in the *Acanthamoeba* SCV. To test this hypothesis, we first evaluated the transcriptional fusion of the *mntH* promoter region to mCherry2 by live-cell imaging (LCI) of *A. castellanii* strain Neff cocultured with Sm18/pSEVA337R_mntH set at a multiplicity of infection of 25 (MOI25) using wide-field fluorescence microscopy. As shown in FIG 9A, the fusion was expressed at 3 and 18 h post-primary contact (ppc). This result strongly suggests that phagocytosed Sm18 cells experience Mn and possibly Fe limitations in the SCV. We used our recently published *A. castellanii*-*Stenotrophomonas* co-culture assay using 96-well microtiter plates coupled to a fluorescence reader (3) to evaluate the replication capacity of the vector integration mutant (VIM) Sm18VIM*mntH* strain and the deleted mutant Sm18Δ*mntR* in

amoebic trophozoites. We tagged Sm18VIM*mntH* and Sm18Δ*mntR* with our pUC18T_mTn7TC1_Pc_mScarlet-I minitransposon, which constitutively expresses the mScarlet-I fluorescent protein from the strong Pc promoter (3), resulting in strains Sm18VIM*mntH*::mTn7_Pc_mScarlet-I and Sm18Δ*mntR*::mTn7_Pc_mScarlet-I (supplementary data, Table 3). The replication capacity of Sm18 tagged with the same transposon (Sm18:: mTn7_Pc_mScarlet-I) in co-culture with Neff trophozoites was compared. As shown in FIG 9B, the Sm18VIM*mntH* mutant had a statistically reduced replication capacity in Neff trophozoites compared to Sm18, whereas Sm18Δ*mntR* exhibited a growth capacity indistinguishable from that of the wild-type strain (FIGS 9B and 9C). These findings support the hypothesis that *Acanthamoeba* phagosomes restrict manganese availability to ingested bacteria and demonstrate that MntH is indispensable for optimal intracellular replication.

DISCUSSION

This study provides new insights into the MntR miniregulon of *Stenotrophomonas maltophilia* and related species in the *S. maltophilia* complex involved in manganese homeostasis, revealing similarities to known systems in other bacteria and novel cell envelope components (FIG 10). As expected, the core elements of the *S. maltophilia* MntR system include the inner-membrane importer and exporter proteins MntH and MntP under the control of the MntR allosteric metalloregulator (FIG 10A), which are highly conserved throughout evolution (24, 43). However, *S. maltophilia* and other *Stenotrophomonas* species also feature a novel bicistronic operon encoding an outer membrane (OM) TonB-dependent receptor (TBDR, V8P17_002357) and a periplasmic thioredoxin-fold protein (pTFP, V8P17_002358; FIG 10B). Gram-negative bacteria typically encode multiple TBDR-like genes, many of which have unknown functions (61, 62). It is well established that in *S. maltophilia,* iron limitation enhances virulence and biofilm formation (29, 63), and the expression of TBDRs involved in heme (64), hemin (65, 66), and ferri-stenobactin (67, 68) uptake, as well as others involved in competition for secreted pyochelin siderophores in mixed cultures with *Pseudomonas aeruginosa* (69). In addition to iron acquisition, *S. maltophilia* TBDRs have been implicated in β-lactam (70) and keratin monomer uptake (71). *Xanthomonas*, the sister genus of *Stenotrophomonas*, features around 70 TBDRs, many of which are required for scavenging plant carbohydrates (61). At least 14 TonB-dependent iron acquisition and virulence pathways

have been extensively studied in *P. aeruginosa* (72). Other well-known TBDRs, such as BtuB, OprC, FhuA, and FecA, translocate vitamin B12 (cyanocobalamin), copper, ferric hydroxamate, and Fe^{3+} dicitrate, respectively. However, MnoT (Q2SY62_BURTA) from *Burkholderia* is the only TBDR currently known to import Mn (28). Analysis of the *S. maltophilia* Sm18 genome (37) revealed that it encodes 65 putative TBDRs, representing one of the most expanded paralogous gene families in this organism (data not shown). Our MEME-MAST analyses (FIG 3B) revealed that V8P27_002357 is the only TBDR associated with an MntR-binding box in Sm18. This box is located 75 bp upstream of the putative start codon, between the -10 and -35 regions (FIG 3B), supporting the notion that MntR is a transcriptional repressor of this locus. Transcriptional fusion and transcriptome profiling data revealed that the *orf2357-orf2358* operon was derepressed only under severe manganese and iron restriction, with its expression virtually abolished upon the addition of 80 nM manganese. This correlates with observations of other TBDRs, typically expressed only under severely limiting nutritional conditions (28, 73), and highlights the interplay of manganese and iron in the unknown regulatory mechanism of the *orf2357-orf2358* locus. However, the Sm18Δ*orf2357* (TBDR) and Sm18Δ*orf2358* deletion mutants did not exhibit a growth phenotype under these nutrient-restricted conditions, and the Sm18/337R-pr_*2357-2358* transcriptional fusion was not expressed in co-cultures with *A. castellanii* trophozoites (data not shown). Phylogenomic analysis of Sm18 TBDRs and a broad collection of well-classified reference proteins from this family revealed that it belongs to a novel clade possibly involved in Mn uptake, which is unrelated to the *Burkholderia* MnoT clade or typical iron-importing TBDRs mentioned above (data not shown). This conclusion is supported by detailed analyses performed on the high-confidence alphaFold3 structural model generated for V8P27_002357. Its most distinguishing feature is the presence of a CQNC motif located at the tip of a loop connecting two antiparallel β-strands protruding from the plug domain toward the cell surface. Based on the bioinformatic and transcriptional evidence gathered, we hypothesized that V8P27_002357 functions as an OM Mn importer. To challenge this hypothesis, we modeled the binding of Mn^{2+} to V8P27_002357 using AlphaFold3 (AF3) (49). A detailed inspection of the high-confidence model predicted that the metal cation is coordinated in a tetrahedral geometry by the two cysteines from the CQNC motif and the spatially neighboring residues E247 and H446 from the β-barrel domain (FIGS 6F-H). Furthermore, the distances of these donor residues to the coordinated metal are within the range of experimentally determined coordination distances in high-resolution (< 1.8 Å) crystal structures collected in the

MESPEUS database of coordination groups in proteins (52) and close to the median distances computed from these structures (FIG 6I). Based on this strong modeling evidence, our current working hypothesis is that, in contrast to the MnoT-like TBDRs of *Burkholderia*, which require the T6SS-4-secreted Mn^{2+}-binding effector TseM to import the Mn^{2+}-TseM complex, in *S. maltophilia,* Mn^{2+} might be directly coordinated in a tetrahedral geometry via the cysteines from the CQNC motif in the plug domain and the E247 and H446 residues from the β-barrel domain. Interestingly, we found that the potential salt bridge forming an ionic lock (IL) in the apoprotein model between R19 and D332 (FIGS 6C-E) could be released upon ligand binding by an allosteric switch (FIGS 6F and 6 J), possibly contributing to substrate import, as reported for the *E. coli* cianocobalamin transporter BtuB (50, 51), an extensively characterized TBDRs with a relatively close phylogenetic relationship to V8P27_002357 (FIG 6K). This model prediction (FIGS 6D, 6E, 6G, and 6J) is consistent with the experimental evidence provided by Hickman et al. via atomic force microscopy that the plug domain of BtuB consists of an N-terminal mechanically weak subdomain. In contrast, the C-terminal subdomain is mechanically strong (74). According to this model, the N-terminal Ton box sequence is exposed upon substrate binding and is accessible for interaction with the periplasmic C-terminal domain (CTD) of the TonB protein, as reported for the *E. coli* BtuB transporter (75) and predicted by our AF3 model (FIGS 6B, 6F, and 6G). It has been proposed that the interaction between the Ton box and the CTD of TonB contributes to partial plug unfolding by the pulling force exerted by the rotation of the inner membrane ExbBD motor (76). Taken together, the excellent fit of our AF3 model predictions with experimental data and models of the TBDR function (50, 51, 73, 77) and the high structure confidence metrics (PAE, pILDT, ipTM, and pTM) lend strong support to our current functional model for V8P27_002357 and highlight the power of current AI protein structure prediction methods to generate highly accurate models and detailed working hypotheses for novel proteins (78). However, experimental evidence is required to validate and refine the model predictions (79). This is particularly important for membrane proteins, such as TBDRs, which establish multiple contacts with neighboring molecules in the densely crowded OM, which can affect folding details (51, 80).

The discovery of a periplasmic thioredoxin-fold protein (pTFP; V8P27_002358) as part of the MntR regulon expands the known components of bacterial manganese homeostasis and thiol-disulfide exchange systems. Furthermore, this finding adds a new layer of complexity to our understanding of how bacteria manage metal homeostasis and oxidative stress in the cell

envelopes. Synteny, phylogenetic co-occurrence (FIG 7A), and co-transcription in a bicistronic operon with the preceding CQNC-type TBDRs suggest a functional coupling between both (V8P27_002357-2358) proteins. It is well established that most secreted proteins enter the periplasm via the Sec pathway in an unfolded form (81). The periplasm of gram-negative bacteria is an oxidizing compartment in which sulfur-containing amino acids, such as cysteine and methionine, are particularly vulnerable to oxidation by ROS (82). Disulfide bond formation in the periplasm of didermic Gammaproteobacteria is catalyzed by DsbA from the canonical DsbAB pathway as the unfolded intermediate transits through the SecYEG channel (83, 84). DsbA is a highly oxidizing soluble periplasmic oxidoreductase with a canonical thioredoxin fold and CXXC motif, which is also present in *S. maltophilia* Sm18 (V8P27_002985, BsbAsm). Therefore, it is likely that the two consecutive cysteines found in CQNC-TBDR are oxidized, forming a disulfide bridge by the action of BsbAsm as it transits into the periplasm through the SecYEG channel. In this model, the cognate and specialized periplasmic thioredoxin-fold protein V8P27_002358 is required to reduce the disulfide bond in the CQNC motifs as the protein folds and integrates into the outer membrane to fulfill its predicted role as a Mn-importing TBDR (FIG 10B). This reduction is required for the two cysteines to participate in metal coordination, as predicted by the AF3 models presented in FIGS 6F-H and discussed above. Therefore, we postulated that V8P27_002358 is a specialized disulfide reductase for the CQNC motif in V8P27_002357. However, assuming this model is correct, it still raises the question of how the oxidized V8P27_002358 protein, after reducing its target's disulfide bond in the CQNC motif, is recycled back into its reduced state. One attractive and likely possibility is that the *S. maltophilia* Sm18 homolog (V8P27_003626; DsbDsm) of the inner membrane protein DsbD catalyzes this reaction. DsbB is a promiscuous protein-disulfide reductase that functions as a redox interaction hub, transferring electrons across the membrane from NADPH and the cytoplasmic Trx system via a cascade of thiol-disulfide exchange reactions to multiple periplasmic thiol-disulfide oxidoreductases (85, 86) belonging to diverse cell envelope reducing pathways (87). This working model for the novel TBDR-pTFP locus (FIG 10B) opens new avenues for research into bacterial metal acquisition strategies and thiol-disulfide homeostasis in the periplasm.

Regarding the conserved and broadly distributed MntR miniregulon components, this study reports the first genetic analysis of *mntH* in *S. maltophilia*. This provides evidence that it encodes its primary manganese importer protein and is relevant for replication in amoebal phagosomes. There are several lines of evidence to support this conclusion. The *mntH* gene

maps downstream of the *mntR* gene. It is regulated by both manganese and iron availability, as shown by our RNA-seq and transcriptional fusion data, and has been observed in *E. coli* and multiple other bacteria (43). Furthermore, transcriptome analysis suggests that no other manganese inner-membrane transporter is solely regulated by manganese availability in Sm18. Perhaps most significantly, *mntH* is reported herein for the first time to be required for *optimal replication of S. maltophilia* within a professional phagocyte, *Acanthamoeba castellanii*. This finding has broader implications for understanding the pathogenicity of S. maltophilia. This suggests that manganese acquisition contributes significantly to bacterial fitness within host cells. We observed active expression of the *mntH* promoter probe *in vivo* in co-cultures with *A. castellanii*. This indicates that Sm18 most likely faces manganese and iron restrictions within amoebal phagosomes. *S. maltophilia*'s ability to overcome these limitations through MntH-mediated manganese import may be a key factor in its success as an intracellular pathogen, as found in other bacteria (88–91), effectively overcoming the host's imposed nutritional immunity (10, 14), an ancient trait of eukaryotic phagocytes conserved from amoebae to macrophages (92). Given that *S. maltophilia*, like most Gammaproteobacteria, is a ferrophilic bacterium (see further discussion below), it is not surprising that the Sm18VIM*mntH* mutant did not display significant impairment when grown in defined MOPS medium without Mn (data not shown). This observation suggests that the attenuated replication rate of this mutant in amoebal phagosomes might be due to its limited capacity to contend with reactive oxygen species (ROS), such as superoxide anions and peroxides (30) (FIG 10C). *S. maltophilia* genomes, including that of Sm18, encode a periplasmic Mn-dependent superoxide dismutase (SOD) and Mn catalase (93). In addition, some enzymes, such as cambialistic SODs (94) or ribonucleotide reductases (47, 95, 96), can use either Fe or Mn as a co-factor, whereas mismetallation or oxidation via Fenton reactions of iron-containing enzymes in metal-restricted environments in the presence of ROS may be alleviated by using Mn as an alternative co-factor, as described for diverse mononuclear iron enzymes, most notably the key enzyme ribulose-5-phosphate 3-epimerase (Rpe) from the pentose-phosphate pathway (PPP) (30, 97, 98). The metallation of Rpe with oxidative stress-resistant Mn^{2+} enables carbon flow through the PPP, producing the NADPH-reducing power required to maintain ROS-countering enzymes, such as glutathione or thioredoxin reductase (99, 100), in the cytoplasm and diverse periplasmic disulfide isomerases and reductases, probably including the novel pTFP-encoding gene discovered herein.

This study did not directly analyze the link between Mn uptake and phagosome ROS contention in *S. maltophilia-A. castellanii* interactions, which is the subject of ongoing research in our laboratory. However, we did not identify any DEGs associated with oxidative stress. This might have resulted from using the wild type rather than a mutant strain lacking manganese exporters.

In this study, we analyzed the links between manganese and iron homeostasis systems, focusing on the genes specifically induced by the former under the control of MntR and iron limitation. However, in addition to the MntR miniregulon members, a few other genes were differentially expressed under iron-replete and manganese excess conditions. As anticipated, the *mntH* and *mntP* genes were expressed differentially. The remaining DEGs uncovered under these conditions require further investigation to validate their potential functions in manganese and iron homeostasis. Of particular relevance was the identification of some efflux pumps of the CDF and RND families, as they have generally been proposed as essential mechanisms for intracellular detoxification of zinc and copper during nutritional immunity (101), when iron and manganese concentrations are likely to be low (FIG 10). Moreover, emerging evidence indicates that an imbalanced ratio of transition metals can function as either a direct or indirect regulatory mechanism to mitigate metal toxicity through efflux pumps. The well-studied YiiP (CDF) has been identified as a secondary transporter for manganese export in Salmonella Typhimurium. Notably, its activity is not regulated by Fe or Mn concentrations in the medium, indicating that YiiP may play a role in balancing the levels of other metals (102). In *Streptococcus pneumoniae*, the expression of *czcD*, a zinc CDF efflux pump, is upregulated under Mn(II)-limiting conditions (103). This is consistent with other studies showing that high zinc concentrations can compete with manganese-binding sites on enzymes essential for cellular physiology (104). In *Bacillus subtilis*, reduced intracellular iron levels heighten cell sensitivity to elevated Co(II) or Mn(II) levels, particularly in strains deficient in exporting these metals (105). Furthermore, disruption of the Mg(II) efflux system alleviates residual manganese toxicity in an *mntR mntH* mutant, likely by preventing mismetallation through Mg(II) accumulation (105, 106). In summary, we hypothesize that under manganese and iron limitation, in addition to uptake systems, other survival mechanisms of Sm18 involve transporters that re-establish the balance of transition metal pools by effluxing the most reactive ones with more favorable free energies (107, 108), thereby preventing mismetallation, as suggested by our integrative model (FIG 10). Our

findings support the importance of maintaining a precise balance of transition metals in bacterial physiology.

In conclusion, our comprehensive analysis of manganese homeostasis in *S. maltophilia* Sm18 revealed a sophisticated network of importers, exporters, and regulatory elements that work coordinately to maintain appropriate intracellular manganese levels. The identification of novel components, such as CQNC-TBDR and pTFP, expands our understanding of bacterial metal homeostasis strategies and opens new avenues for future studies. These findings advance our knowledge of *S. maltophilia* biology and contribute to the broader field of bacterial metal homeostasis, potentially opening new strategies to combat infections by this opportunistic pathogen.

MATERIALS AND METHODS

Bacterial strains and culture conditions *Stenotrophomonas maltophilia* ESTM1D_MKCAZ16_6a (Sm18) was isolated from the sediments of the Las Estacas River in Morelos, Mexico (109). Sm18 was routinely cultivated under aerobic conditions in Luria-Bertani broth (10 g peptone, 5 g yeast extract, and 10 g NaCl in 1 L distilled water) at 30°C and 205 rpm or in MOPS, previously proven effective for cultivating *Pseudomonas* strains using 0.4 % (w/v) glucose as the carbon source (110). We optimized minimal medium MOPS (MM) for *S. maltophilia* growth by adding thiamine and biotin at 0.5% and 0.1% (w/v), respectively, along with 0.2% (w/v) Bacto™ casamino acids (CAA) to improve the growth. Unlike the standard MM recipe, our MM lacks manganese in the micronutrient stock, as previous experiments in our laboratory have shown that nanomolar manganese concentrations do not affect Sm18 growth. For the growth kinetics, the LB medium was supplemented with 10mM of MOPS buffer to maintain the pH above 6.5 after adding millimolar concentrations of manganese. The growth of Sm18 remained unaffected at this buffer concentration and pH (data not shown). We cultured bacteria in MM supplemented with 30 µg/mg chloramphenicol for fluorescence kinetic analyses to select for plasmid pSEVA327.

Generation of markerless deletion mutants Two genomic DNA fragments located upstream and downstream of the *mntP* gene were amplified by PCR using total DNA from Sm18 as the template. The primer pair Sm18DmntP_PCR1.FOR and

Sm18DmntP_PCR1.REV yielded a 570 bp fragment, whereas the pair Sm18DmntP_PCR2.FOR and Sm18DmntP_PCR2.REV produces a 512 pb fragment. These fragments were subsequently cloned into the pEX18Tc vector (111), previously linearized with EcoRI and HindIII, using NEBuilder HiFi DNA Assembly Master Mix (New England Biolabs, NEB), following the manufacturer's instructions. Ten microliters of the resulting NEBuilder reaction was used to transform 50 µL of *E. coli* DH5α by heat shock. Positive transformants were selected using blue-white screening and confirmed by PCR using the primers Sm18DmntP_PCR1.FOR and Sm18DmntP_PCR2.Rev, which amplified a 1082 bp fragment. Finally, the plasmid was purified and linearized to confirm the size difference between the empty vector control and pEX18Tc::DmntP. The suicide vector pEX18Tc::DmntP was introduced into Sm18 by conjugation with *E. coli* S17 to obtain Sm18 merodiploids. The selection of Sm18 merodiploids was carried out using LB media supplemented with 20 µg/mL tetracycline and 30 µg/mL gentamicin and verified by colony PCR using a pair of primers, F24 and Sm18_VIM_mntP.R, which amplify the region from the insert plasmid to the genomic DNA of Sm18. For the second homologous recombination, Sm18 merodiploids were grown in LB without NaCl and supplemented with 10% sucrose directly from glycerol. Marker-less deletion mutants were confirmed by tetracycline sensitivity, colony PCR using the primers Sm18DmntP_VER.F and Sm18DmntP_VER.R that amplified 1131 bp in Sm18 wild type and 570pb in Sm18Δ*mntP* mutant, and by sequencing. The same procedure was used to generate markless TBDR, pTFP, and mntH gene deletion mutants. Details of the vectors and primers are provided in Supplementary Tables S4, S5, and S6.

Development of Interrupted Mutants A DNA fragment from the coding region of the *mntP* gene was amplified by PCR using total DNA from *Sm18* as the template. The primers Sm18-VIM-mntP. F1 and Sm18-VIM-mntP.R1 generated a 401 bp fragment that was cloned into the pEX18Tc Δ SacB-GFP plasmid. The insert and vector were linearized using BamHI and HindIII, followed by T4 DNA ligase (NEB) ligation, according to the manufacturer's protocol. To introduce the construct, 10 µL of the ligation mix was used to transform 50 µL of *E. coli* DH5α by heat shock. Transformants were selected through blue-white screening, and the pEX18TcΔSacB-GFP_DmntP vector was verified by PCR using universal primers F24 and R24, which amplified a 522 bp fragment flanking the insert. For additional confirmation, the vector was purified and linearized, and its size was compared to that of the empty vector control. The suicide vector pEX18TcΔSacB-GFP_DmntP was then introduced into *Sm18* by

conjugation with *E. coli* S17, as described previously. The same procedure was used to generate interrupted mutants of the *TBDR* and *mntH*. Details of the vectors and primers are presented in Supplementary Tables S4, S5, and 6.

Construction of Sm18 expression plasmids We employed empty backbone bacterial expression plasmids from the pSEVA vector collection (112) for the construction of pSEVA327 and pSEVA337R bacterial expression plasmids, both of which harbored cassettes conferring chloramphenicol resistance. The former features an oriVRK2 that facilitates replication at a low copy number across a broad host spectrum. It is replicated and maintained in most gram-negative bacteria, and the cargo is a GFP expression module that lacks a promoter and is therefore well-suited for constructing expression plasmids. The latter encompasses an oriVpBBR1 of medium copy number and an mCherry expression module. Both contain an oriT that allows their transfer by conjugation, if required. The intergenic areas of V8P27_002357, *mntH,* and *mntP* were amplified by PCR from genomic DNA using Phusion polymerase (NEB) and primers flanking 50-150 base pairs upstream and downstream, tagged with a restriction enzyme site for *Eco*RI, *Bam*HI, or *Hind*III. Subsequently, the vectors and amplicons were digested and ligated with T4 DNA polymerase (NEB) to generate Sm18 expression plasmids 327-*TBDR_pTFP*, 327-*mntH*, 327-*mntP*, 337R-*TBDR_pTFP*, 337R-*mntH,* and 337R-*mntP*. See details of vectors and primers in supplementary Tables S4, S5 and S6.

Fluorescence kinetics and microbial growth The Fluorescence and growth kinetics were assessed across three or more biological replicates in a 96-well microplate. The bacterial optical density (OD_{600}) was adjusted to 0.05 in LB and 0.01 in MM at a final volume of 200 µL of medium and supplemented with increasing $MnCl_2$ concentrations. For growth kinetics, cultures were grown at 30°C with orbital shaking at 205 rpm in a Biotek Epoch 2 microplate spectrophotometer, with OD_{600} readings taken every 30 or 45 min. The same setup was used for fluorescence kinetics analysis, with fluorescence and growth measurements recorded using a BioTek Synergy H1 hybrid multi-mode microplate reader. The excitation and emission spectra for green fluorescent protein (GFP) were set at 479/12.5 nm and 520/12.5 nm, respectively.

Statistical analysis of fluorescence and growth kinetics For microbial growth curves, an uninoculated medium served as the blank. For the fluorescence curves, in addition to

subtracting the blank, normalization to microbial growth was also conducted. The non-parametric Kruskal-Wallis test was used to compare the medians across independent groups based on the Area Under the Curve (AUC) derived from the growth or fluorescence measurements of Sm18 (or the specific strain/experiment name) to assess the overall statistical significance. When significant differences were detected, *post hoc* pairwise comparisons were performed using Dunn's test. The resulting *p*-values were adjusted for multiple comparisons using either the Bonferroni or Benjamini-Hochberg (BH) method, as appropriate. Significant contrast values are indicated by asterisks (*) in the figures. The significance levels are as follows: $p > 0.05$ = ns (not significant); $p < 0.05$ = *; $p < 0.01$ = **; $p < 0.001$ = ***; $p < 0.0001$ = ****). The AUC was calculated using the Growthcurver package (v. 0.3.1). Bootstrapping was employed on the AUC data to compute 95% confidence intervals, which are represented as error bars in the corresponding figure. The rstatix package (v 0.7.2) was used to perform statistical tests. All statistical analyses and graph generation were conducted using the R programming language (v 4.3.2). Data variability was visualized using the ggplot2 (v 3.5.1) and ggpubr package (v 4.3.2). Error bars on the growth kinetic graphs represent the standard error of the mean for the technical and biological replicates.

Cell sample preparation for RNA-sequencing Three biological replicates were obtained from glycerol stored at -80°C and cultured on LB agar to isolate colonies, with a one-day interval between each replicate. The cultures were then incubated at 30°C for 34 h. Subsequently, a single isolated colony was subcultured in 3 mL of MM and incubated at 30°C with agitation at 205 rpm for 24 h. For pre-culturing, a 1:50 dilution was made in a final volume of 25 mL of MM in a 50 ml Erlenmeyer flask and incubated at 30°C with shaking at 205 rpm for 14 h. Following pre-culturing, 10 mL of the pre-culture was collected by centrifugation (5000 × g for 5 min), washed three times with 5 mL of MM without Fe (MM-Fe0), and resuspended in 5 mL of the same culture medium. This preculture was then used to inoculate 25 ml of four different micromolar metal-supplemented MM media cultures at OD_{600} ~ 0.005: MM-Fe0Mn0, MM-Fe0Mn8, MM-Fe10Mn0, and MM-Fe10Mn8. For all conditions, Sm18 was incubated at 30 °C/205 rpm until reaching the early log phase (OD_{600} 0.1 -0.2), after which the cultures were divided into two technical replicates, and the cells were harvested by centrifugation as previously described. Immediately, the pellets were covered with 900µL of RNA later. One technical replica was stored at 4°C until it was shipped to GENEWIZ from Azenta Life Science for library preparation and sequencing. The other was

stored at -80°C for subsequent experiments. Standard RNA-seq was performed on an Illumina HiSeq 2500 platform, resulting in 150 bp paired-end reads.

RNA-seq analysis data and gene expression After read quality assessment using Fastqc v 0.12.1 (113), we employed Trimmomatic v 0.39 (114) to trim the index adapter and the initial 15 bp from each read, resulting in 135 bp reads and more than 23 million paired-end reads per sample. The complete genome sequence of *Stenotrophomonas maltophilia* strain ESTM1D_MKCAZ16_6a (BioProject: PRJNA1081934) served as a reference for aligning the reads using Bowtie2 v 2.4.4 (115). The aligned SAM files generated by Bowtie2 (overall alignment rate per sample >96%) were then used as input for featuresCounts from the R-Bioconductor software package Rsubreads v 2.14.2 (116). FeaturesCount generated an expression matrix containing the expression values of each sample for every gene using the GFF genome annotation file (successfully assigned alignments per sample >92%). Differential gene expression analysis between conditions (Fe10Mn0 vs. Fe10Mn8, Fe0Mn0 vs. Fe0Mn8, Fe10Mn0 vs. Fe0Mn0, and Fe10Mn8 vs. Fe0Mn8) was performed using DESeq2 v 1.42.0 (117), R-Bioconductor package, which normalizes the raw counts through the median of ratios method and conducts differential expression analysis based on the negative binomial distribution of the data. DESeq2 adjusted P-values using Benjamini and Hochberg's method were used to reduce the false discovery rate. Differentially expressed genes (DEGs) were identified using the adjusted P-value (Padj) < 0.05 and log2 fold change > 1 or < -1 as cutoffs. The protein sequences of DGEs in response to Mn^{2+} stress under both iron-deficient and iron-supplemented conditions were analyzed using the UniProt database (118), InterProScan (119), and MOTIF search (https://www.genome.jp/tools/motif/) to assign functions and Gene Ontology (GO) terms.

Identification of transcription factor binding sites and protein homologs We used the motif discovery algorithm MEME (v 5.5.5) from the MEME suite (42) to identify statistically overrepresented sequence motifs between 16 and 25 nt long, located in the 5' UTR regions of *Stenotrophomonas mntH* (V8P27_002360) orthologs identified with GET_HOMOLOGUES (46). The resulting position-specific probability matrices (PSPMs) were compared with entries in the CollecTF (120) and PRODORIC (121) databases of experimentally validated transcription factor-binding sites in bacteria using TOMTOM (v 5.5.5) from the MEME suite to

determine the identity of the discovered motifs. The collection of 5' UTR regions containing the MntR-box motif was extended by adding new hits discovered by MAST (v 5.5.5) scans of complete genome sequences representative of the currently described taxonomic diversity of *Stenotrophomonas* and related genera in the *Lysobacteriaceae* (39, 45). Homologs of the *S. maltophilia* MntR miniregulon proteins were identified by hmmsearch (v3.4) from the HMMER3 suite (44) using the gathering threshold (--cut_ga option) for calibrated profile hidden Markov models (HMMs) retrieved from Pfam (PF01566 for MntH, PF02659 for MntP), or built locally with hmmbuild (v3.4) from clustal omega (122) alignments (with –iter 2 and –use-kimura options) of our curated datasets of MntR, V8P27_002357, and V8P27_002358 homologs. The Latter three HMMs and the PSPM for the *Lisobacteraceae* MntR-box are available for download from https://github.com/vinuesa/supplementary_materials/.

Live-cell imaging (LCI) using widefield fluorescence microscopy of Sm18/337R-*mntH* in co-culture with *Acanthamoeba castellanii* The detailed description of the co-culture procedure is found in Rivera 2024 (3). Briefly, co-cultures were established by seeding 20-mm diameter glass-bottom cell culture dishes with 5×10^5 *Acanthamoeba castellanii* strain Neff trophozoites, which were incubated for 1 h at 30°C in MMsalts-MOPS-Glc medium. *Stenotrophomonas maltophilia* Sm18/337R-*mntH* was grown in LB medium, washed, and adjusted to an OD_{600} of ~1.0 (~4.8×10^8 CFU/mL). Diluted bacterial suspensions were added to the culture dishes to achieve a multiplicity of infection (MOI) of 25, followed by centrifugation at 500 × g for 5 min to synchronize phagocytosis. LCI was performed using an AxioVertA1 inverted microscope (Karl Zeiss) at three and 18 h ppc.

Quantitative evaluation of the intracellular replication of mutant strains Sm18VIM*mntH* and Sm18Δ*mntR* in Acanthamoeba trophozoites. Experiments were performed using a microtiter plate assay**, as described** by Rivera (2024) (3). To evaluate the intracellular replication of the mutants Sm18VIM*mntH*::mTn7_Pc_mScarlet-I and Sm18Δ*mntR*::mTn7_Pc_mScarlet-I in *Acanthamoeba* trophozoites at MOI10, we used a microtiter plate assay that measured mScarlet-I fluorescence of the bacterial strains in co-cultures. Each well contained 1×10^5 trophozoites in MMsalts-MOPS-Glc and was incubated for 30 min at 25°C. After replacing the medium with the tagged bacteria at the desired MOI, phagocytosis was synchronized by centrifugation at 500 × g for 5 min. The

plates were then placed in a plate reader Synergy 2 and incubated statically at 25°C. Red fluorescence was measured every 30 min for 48 h at 568 nm/594 nm (excitation/emission). The controls included wells with medium, trophozoites in the medium, or bacteria in the medium.

ACKNOWLEDGEMENTS

We thank Alfredo Hernández and Víctor del Moral for their expert technical support and server maintenance at the Centro de Ciencias Genómicas, UNAM. We acknowledge the excellent service provided by personnel at the Unidad de Síntesis y Secuenciación de DNA from Instituto de Biotecnología, UNAM. We thank Dr. Ayari Fuentes from CCG-UNAM for providing access to the multimodal plate reader. We thank Dr. Luis Lozano from the Bioinformatics Unit at CCG-UNAM for his advice and support during the early phase of transcriptome analysis. We thank M.Sc. Laura Cervantes for her laboratory assistance and valuable feedback. We gratefully acknowledge the financial support received from Consejo Nacional de Humanidades Ciencias y Tecnologías (CONAHCyT México, A1-S-11242), Secretaría de Ciencia, Humanidades, Tecnología e Innovación (SECIHTI México CBF-2025-I-1106), and Programa de Apoyo a Proyectos de Investigación e Innovación Tecnológica (PAPIIT), Universidad Nacional Autónoma de México (DGAPA-PAPIIT, UNAM: IN209321 and IN216424) to PV. F. S. A. Z. and J.C.V.N. were recipients of CONAHCyT scholarships 659308 and 745705, respectively.

REFERENCES

1. Brooke JS. 2021. Advances in the Microbiology of Stenotrophomonas maltophilia. Clin Microbiol Rev 34:e00030-19.

2. Ryan RP, Monchy S, Cardinale M, Taghavi S, Crossman L, Avison MB, Berg G, Van Der Lelie D, Dow JM. 2009. The versatility and adaptation of bacteria from the genus Stenotrophomonas. Nat Rev Microbiol 7:514–525.

3. Rivera J, Valerdi-Negreros JC, Vázquez-Enciso DM, Argueta-Zepeda F-S, Vinuesa P. 2024. Phylogenomic, structural, and cell biological analyses reveal that *Stenotrophomonas maltophilia* replicates in acidified Rab7A-positive vacuoles of *Acanthamoeba castellanii*. Microbiol Spectr 12:e02988-23.

4. Ochoa-Sánchez LE, Vinuesa P. 2017. Evolutionary Genetic Analysis Uncovers Multiple Species with Distinct Habitat Preferences and Antibiotic Resistance Phenotypes in the Stenotrophomonas maltophilia Complex. Front Microbiol 8:1548.

5. Brooke JS. 2012. Stenotrophomonas maltophilia: an Emerging Global Opportunistic Pathogen. Clin Microbiol Rev 25:2–41.

6. Rello J, Kalwaje Eshwara V, Lagunes L, Alves J, Wunderink RG, Conway-Morris A, Rojas JN, Alp E, Zhang Z. 2019. A global priority list of the TOp TEn resistant Microorganisms (TOTEM) study at intensive care: a prioritization exercise based on multi-criteria decision analysis. Eur J Clin Microbiol Infect Dis 38:319–323.

7. Chang Y-T, Lin C-Y, Chen Y-H, Hsueh P-R. 2015. Update on infections caused by Stenotrophomonas maltophilia with particular attention to resistance mechanisms and therapeutic options. Front Microbiol 6.

8. Denet E, Vasselon V, Burdin B, Nazaret S, Favre-Bonté S. 2018. Survival and growth of Stenotrophomonas maltophilia in free-living amoebae (FLA) and bacterial virulence properties. PLoS ONE 13:e0192308.

9. Takahashi I, Hosomi K, Nagatake T, Toubou H, Yamamoto D, Hayashi I, Kurashima Y, Sato S, Shibata N, Goto Y, Maruyama F, Nakagawa I, Kuwae A, Abe A, Kunisawa J, Kiyono H. 2020. Persistent colonization of non-lymphoid tissue-resident macrophages by *Stenotrophomonas maltophilia*. International Immunology 32:133–141.

10. Murdoch CC, Skaar EP. 2022. Nutritional immunity: the battle for nutrient metals at the host-pathogen interface. Nat Rev Microbiol 20:657–670.

11. Palmer LD, Skaar EP. 2016. Transition Metals and Virulence in Bacteria. Annu Rev Genet 50:67–91.

12. Waldron KJ, Robinson NJ. 2009. How do bacterial cells ensure that metalloproteins get the correct metal? Nat Rev Microbiol 7:25–35.

13. Porcheron G, Garénaux A, Proulx J, Sabri M, Dozois CM. 2013. Iron, copper, zinc, and manganese

transport and regulation in pathogenic Enterobacteria: correlations between strains, site of infection and the relative importance of the different metal transport systems for virulence. Front Cell Infect Microbiol 3.

14. Chandrangsu P, Rensing C, Helmann JD. 2017. Metal homeostasis and resistance in bacteria. Nat Rev Microbiol 15:338–350.

15. Rahil-Khazen R, Bolann BJ, Myking A, Ulvik RJ. 2002. Multi-element analysis of trace element levels in human autopsy tissues by using inductively coupled atomic emission spectrometry technique (ICP-AES). Journal of Trace Elements in Medicine and Biology 16:15–25.

16. Kehl-Fie TE, Zhang Y, Moore JL, Farrand AJ, Hood MI, Rathi S, Chazin WJ, Caprioli RM, Skaar EP. 2013. MntABC and MntH Contribute to Systemic Staphylococcus aureus Infection by Competing with Calprotectin for Nutrient Manganese. Infect Immun 81:3395–3405.

17. Versieck J, Barbier F, Speecke A, Hoste J. 1974. Manganese, copper, and zinc concentrations in serum and packed blood cells during acute hepatitis, chronic hepatitis, and posthepatitic cirrhosis. Clin Chem 20:1141–1145.

18. Pompilio A, Ciavardelli D, Crocetta V, Consalvo A, Zappacosta R, Di Ilio C, Di Bonaventura G. 2014. Stenotrophomonas maltophilia Virulence and Specific Variations in Trace Elements during Acute Lung Infection: Implications in Cystic Fibrosis. PLoS ONE 9:e88769.

19. Mikhailovich V, Heydarov R, Zimenkov D, Chebotar I. 2024. Stenotrophomonas maltophilia virulence: a current view. Front Microbiol 15:1385631.

20. Song F, Zhang G, Li H, Ma L, Yang N. 2022. Comparative transcriptomic analysis of Stenotrophomonas sp. MNB17 revealed mechanisms of manganese tolerance at different concentrations and the role of histidine biosynthesis in manganese removal. Ecotoxicology and Environmental Safety 244:114056.

21. Bosma EF, Rau MH, van Gijtenbeek LA, Siedler S. 2021. Regulation and distinct physiological roles of manganese in bacteria. FEMS Microbiology Reviews 45:fuab028.

22. Waters LS. 2020. Bacterial manganese sensing and homeostasis. Current Opinion in Chemical Biology

55:96–102.

23. Kehres DG, Zaharik ML, Finlay BB, Maguire ME. 2000. The NRAMP proteins of *Salmonella typhimurium* and *Escherichia coli* are selective manganese transporters involved in the response to reactive oxygen. Molecular Microbiology 36:1085–1100.

24. Waters LS, Sandoval M, Storz G. 2011. The Escherichia coli MntR Miniregulon Includes Genes Encoding a Small Protein and an Efflux Pump Required for Manganese Homeostasis. J Bacteriol 193:5887–5897.

25. Wright Z, Seymour M, Paszczak K, Truttmann T, Senn K, Stilp S, Jansen N, Gosz M, Goeden L, Anantharaman V, Aravind L, Waters LS. 2024. The small protein MntS evolved from a signal peptide and acquired a novel function regulating manganese homeostasis in *Escherichia coli*. Molecular Microbiology 121:152–166.

26. Sengupta S, Mondal A, Dutta D, Parrack P. 2018. HflX protein protects Escherichia coli from manganese stress. J Biosci 43:1001–1013.

27. Que Q, Helmann JD. 2000. Manganese homeostasis in *Bacillus subtilis* is regulated by MntR, a bifunctional regulator related to the diphtheria toxin repressor family of proteins. Molecular Microbiology 35:1454–1468.

28. Si M, Zhao C, Burkinshaw B, Zhang B, Wei D, Wang Y, Dong TG, Shen X. 2017. Manganese scavenging and oxidative stress response mediated by type VI secretion system in *Burkholderia thailandensis*. Proc Natl Acad Sci USA 114.

29. Kalidasan V, Joseph N, Kumar S, Awang Hamat R, Neela VK. 2018. Iron and Virulence in Stenotrophomonas Maltophilia: All We Know So Far. Front Cell Infect Microbiol 8:401.

30. Anjem A, Varghese S, Imlay JA. 2009. Manganese import is a key element of the OxyR response to hydrogen peroxide in *Escherichia coli*. Molecular Microbiology 72:844–858.

31. Čapek J, Večerek B. 2023. Why is manganese so valuable to bacterial pathogens? Front Cell Infect Microbiol 13:943390.

32. Zhang T, Wu H, Ma C, Yang Y, Li H, Yang Z, Zhou S, Shi D, Chen T, Yang D, Li J, Jin M. 2024. Emergence of colistin-resistant Stenotrophomonas maltophilia with high virulence in natural aquatic environments. Science of The Total Environment 933:173221.

33. Nas MY, White RC, DuMont AL, Lopez AE, Cianciotto NP. 2019. Stenotrophomonas maltophilia Encodes a VirB/VirD4 Type IV Secretion System That Modulates Apoptosis in Human Cells and Promotes Competition against Heterologous Bacteria, Including Pseudomonas aeruginosa. Infect Immun 87:e00457-19.

34. DuMont AL, Karaba SM, Cianciotto NP. 2015. Type II Secretion-Dependent Degradative and Cytotoxic Activities Mediated by Stenotrophomonas maltophilia Serine Proteases StmPr1 and StmPr2. Infect Immun 83:3825–3837.

35. Juttukonda LJ, Skaar EP. 2015. Manganese homeostasis and utilization in pathogenic bacteria. Molecular Microbiology 97:216–228.

36. Cellier M. 2001. Polyphyletic origins of bacterial Nramp transporters. Trends in Genetics 17:365–370.

37. Vinuesa P, Fulvia-Stefany A-Z, Luz Edith O-S, Julio C. V-N, Mauricio D. O-H, Daniela G-H, Diana M. V-E, Javier R. 2024. Complete genome sequence of the environmental Stenotrophomonas maltophilia ESTM1D_MKCAZ16_6a (Sm18) strain recovered from sediments of a clean river in Morelos. Mexico, MRA.

38. Tatusova T, DiCuccio M, Badretdin A, Chetvernin V, Nawrocki EP, Zaslavsky L, Lomsadze A, Pruitt KD, Borodovsky M, Ostell J. 2016. NCBI prokaryotic genome annotation pipeline. Nucleic Acids Res 44:6614–6624.

39. Vinuesa P, Ochoa-Sánchez LE, Contreras-Moreira B. 2018. GET_PHYLOMARKERS, a Software Package to Select Optimal Orthologous Clusters for Phylogenomics and Inferring Pan-Genome Phylogenies, Used for a Critical Geno-Taxonomic Revision of the Genus Stenotrophomonas. Front Microbiol 9:771.

40. Zeinert R, Martinez E, Schmitz J, Senn K, Usman B, Anantharaman V, Aravind L, Waters LS. 2018.

Structure–function analysis of manganese exporter proteins across bacteria. Journal of Biological Chemistry 293:5715–5730.

41. Patzer SI, Hantke K. 2001. Dual Repression by Fe $^{2+}$ -Fur and Mn $^{2+}$ -MntR of the *mntH* Gene, Encoding an NRAMP-Like Mn $^{2+}$ Transporter in *Escherichia coli*. J Bacteriol 183:4806–4813.

42. Bailey TL, Johnson J, Grant CE, Noble WS. 2015. The MEME Suite. Nucleic Acids Res 43:W39–W49.

43. Martin JE, Waters LS. 2022. Regulation of Bacterial Manganese Homeostasis and Usage During Stress Responses and Pathogenesis. Front Mol Biosci 9:945724.

44. Eddy SR. 2011. Accelerated Profile HMM Searches. PLoS Comput Biol 7:e1002195.

45. Chauviat A, Abrouk D, Brothier E, Muller D, Meyer T, Favre-Bonté S. 2025. Genomic and phylogenetic re-assessment of the genus Stenotrophomonas: Description of Stenotrophomonas thermophila sp. nov., and the proposal of Parastenotrophomonas gen. Nov., Pseudostenotrophomonas gen. Nov., Pedostenotrophomonas gen. Nov., and Allostenotrophomonas gen. Nov. Syst Appl Microbiol 48:126630.

46. Contreras-Moreira B, Vinuesa P. 2013. GET_HOMOLOGUES, a Versatile Software Package for Scalable and Robust Microbial Pangenome Analysis. Appl Environ Microbiol 79:7696–7701.

47. Wang NE, Courcelle EJ, Coltman SM, Spolek RL, Courcelle J, Courcelle CT. 2023. Manganese transporters regulate the resumption of replication in hydrogen peroxide-stressed Escherichia coli. Biometals 36:1361–1376.

48. Taudte N, German N, Zhu Y-G, Grass G, Rensing C. 2016. Restoration of growth by manganese in a mutant strain of Escherichia coli lacking most known iron and manganese uptake systems. Biometals 29:433–450.

49. Abramson J, Adler J, Dunger J, Evans R, Green T, Pritzel A, Ronneberger O, Willmore L, Ballard AJ, Bambrick J, Bodenstein SW, Evans DA, Hung C-C, O'Neill M, Reiman D, Tunyasuvunakool K, Wu Z, Žemgulytė A, Arvaniti E, Beattie C, Bertolli O, Bridgland A, Cherepanov A, Congreve M, Cowen-Rivers AI, Cowie A, Figurnov M, Fuchs FB, Gladman H, Jain R, Khan YA, Low CMR, Perlin K, Potapenko A, Savy P,

Singh S, Stecula A, Thillaisundaram A, Tong C, Yakneen S, Zhong ED, Zielinski M, Žídek A, Bapst V, Kohli P, Jaderberg M, Hassabis D, Jumper JM. 2024. Accurate structure prediction of biomolecular interactions with AlphaFold 3. Nature 1–3.

50. Zmyslowski AM, Baxa MC, Gagnon IA, Sosnick TR. 2022. HDX-MS performed on BtuB in E. coli outer membranes delineates the luminal domain's allostery and unfolding upon B12 and TonB binding. Proc Natl Acad Sci U S A 119:e2119436119.

51. Nilaweera TD, Nyenhuis DA, Cafiso DS. 2021. Structural intermediates observed only in intact Escherichia coli indicate a mechanism for TonB-dependent transport. Elife 10:e68548.

52. Lin G-Y, Su Y-C, Huang YL, Hsin K-Y. 2024. MESPEUS: a database of metal coordination groups in proteins. Nucleic Acids Res 52:D483–D493.

53. Nilewski S, Varatnitskaya M, Masuch T, Kusnezowa A, Gellert M, Baumann AF, Lupilov N, Kusnezow W, Koch M-H, Eisenacher M, Berkmen M, Lillig CH, Leichert LI. 2021. Functional metagenomics of the thioredoxin superfamily. J Biol Chem 296:100247.

54. Martin JL. 1995. Thioredoxin--a fold for all reasons. Structure 3:245–250.

55. Atkinson HJ, Babbitt PC. 2009. An atlas of the thioredoxin fold class reveals the complexity of function-enabling adaptations. PLoS Comput Biol 5:e1000541.

56. Anjou C, Lotoux A, Morvan C, Martin-Verstraete I. 2024. From ubiquity to specificity: The diverse functions of bacterial thioredoxin systems. Environ Microbiol 26:e16668.

57. Quan S, Schneider I, Pan J, Von Hacht A, Bardwell JCA. 2007. The CXXC motif is more than a redox rheostat. J Biol Chem 282:28823–28833.

58. Mavridou DAI, Saridakis E, Kritsiligkou P, Mozley EC, Ferguson SJ, Redfield C. 2014. An extended active-site motif controls the reactivity of the thioredoxin fold. J Biol Chem 289:8681–8696.

59. Peracino B, Buracco S, Bozzaro S. 2013. The Nramp (Slc11) proteins regulate development, resistance to

pathogenic bacteria and iron homeostasis in Dictyostelium discoideum. J Cell Sci 126:301–311.

60. Morey JR, McDevitt CA, Kehl-Fie TE. 2015. Host-imposed manganese starvation of invading pathogens: two routes to the same destination. Biometals 28:509–519.

61. Blanvillain S, Meyer D, Boulanger A, Lautier M, Guynet C, Denancé N, Vasse J, Lauber E, Arlat M. 2007. Plant Carbohydrate Scavenging through TonB-Dependent Receptors: A Feature Shared by Phytopathogenic and Aquatic Bacteria. PLoS ONE 2:e224.

62. Schauer K, Rodionov DA, De Reuse H. 2008. New substrates for TonB-dependent transport: do we only see the 'tip of the iceberg'? Trends in Biochemical Sciences 33:330–338.

63. García CA, Alcaraz ES, Franco MA, Passerini de Rossi BN. 2015. Iron is a signal for Stenotrophomonas maltophilia biofilm formation, oxidative stress response, OMPs expression, and virulence. Front Microbiol 6:926.

64. Shin HE, Pan C, Curran DM, Bateman TJ, Chong DHY, Ng D, Shah M, Moraes TF. 2024. Prevalence of Slam-dependent hemophilins in Gram-negative bacteria. J Bacteriol 206:e0002724.

65. Liao C-H, Lu H-F, Yang C-W, Yeh T-Y, Lin Y-T, Yang T-C. 2024. HemU and TonB1 contribute to hemin acquisition in Stenotrophomonas maltophilia. Front Cell Infect Microbiol 14:1380976.

66. Shih Y-L, Wu C-M, Lu H-F, Li L-H, Lin Y-T, Yang T-C. 2022. Involvement of the *hemP-hemA-smlt0796-smlt0797* Operon in Hemin Acquisition by Stenotrophomonas maltophilia. Microbiol Spectr 10:e00321-22.

67. Wu C-M, Li L-H, Lin Y-L, Wu C-J, Lin Y-T, Yang T-C. 2022. The sbiTRS Operon Contributes to Stenobactin-Mediated Iron Utilization in Stenotrophomonas maltophilia. Microbiol Spectr 10:e0267322.

68. Yeh T-Y, Lu H-F, Li L-H, Lin Y-T, Yang T-C. 2025. Contribution of fepAsm, fciABC, sbaA, sbaBCDEF, and feoB to ferri-stenobactin acquisition in Stenotrophomonas maltophilia KJ. BMC Microbiol 25:91.

69. Pan S-Y, Shih Y-L, Huang H-H, Li L-H, Lin Y-T, Yang T-C. 2022. The involvement of PacIRA system of

Stenotrophomonas maltophilia in the uptake of Pseudomonas aeruginosa pyochelin and intraspecies competition for iron acquisition. Journal of Microbiology, Immunology and Infection 55:273–281.

70. Calvopiña K, Dulyayangkul P, Heesom KJ, Avison MB. 2020. TonB-dependent uptake of β-lactam antibiotics in the opportunistic human pathogen Stenotrophomonas maltophilia. Mol Microbiol 113:492–503.

71. Xue K, Song X, Zhang W, Zhang Y, Chen T, Cao Z, Hong F, Zhang X. 2024. Omics-Based Investigation on Mechanisms Controlling Cellular Internalization of Keratin Monomers during Biodegradation by Stenotrophomonas maltophilia DHHJ. Microb Physiol 34:170–181.

72. Hubert T, Madec M, Schalk IJ. 2023. Experimental and computational methods to highlight behavioural variations in TonB-dependent transporter expression in Pseudomonas aeruginosa versus siderophore concentration. Sci Rep 13:20015.

73. Silale A, Van Den Berg B. 2023. TonB-Dependent Transport Across the Bacterial Outer Membrane. Annu Rev Microbiol 77:67–88.

74. Hickman SJ, Cooper REM, Bellucci L, Paci E, Brockwell DJ. 2017. Gating of TonB-dependent transporters by substrate-specific forced remodelling. Nat Commun 8:14804.

75. Shultis DD, Purdy MD, Banchs CN, Wiener MC. 2006. Outer membrane active transport: structure of the BtuB:TonB complex. Science 312:1396–1399.

76. Ratliff AC, Buchanan SK, Celia H. 2022. The Ton Motor. Front Microbiol 13:852955.

77. Braun V. 2024. Substrate Uptake by TonB-Dependent Outer Membrane Transporters. Mol Microbiol 122:929–947.

78. Akdel M, Pires DEV, Pardo EP, Jänes J, Zalevsky AO, Mészáros B, Bryant P, Good LL, Laskowski RA, Pozzati G, Shenoy A, Zhu W, Kundrotas P, Serra VR, Rodrigues CHM, Dunham AS, Burke D, Borkakoti N, Velankar S, Frost A, Basquin J, Lindorff-Larsen K, Bateman A, Kajava AV, Valencia A, Ovchinnikov S, Durairaj J, Ascher DB, Thornton JM, Davey NE, Stein A, Elofsson A, Croll TI, Beltrao P. 2022. A structural

biology community assessment of AlphaFold2 applications. Nat Struct Mol Biol 29:1056–1067.

79. Terwilliger TC, Liebschner D, Croll TI, Williams CJ, McCoy AJ, Poon BK, Afonine PV, Oeffner RD, Richardson JS, Read RJ, Adams PD. 2024. AlphaFold predictions are valuable hypotheses and accelerate but do not replace experimental structure determination. Nat Methods 21:110–116.

80. Nyenhuis DA, Nilaweera TD, Cafiso DS. 2020. Native Cell Environment Constrains Loop Structure in the Escherichia coli Cobalamin Transporter BtuB. Biophys J 119:1550–1557.

81. Smets D, Loos MS, Karamanou S, Economou A. 2019. Protein Transport Across the Bacterial Plasma Membrane by the Sec Pathway. Protein J 38:262–273.

82. Collet J-F, Cho S-H, Iorga BI, Goemans CV. 2020. How the assembly and protection of the bacterial cell envelope depend on cysteine residues. J Biol Chem 295:11984–11994.

83. Kadokura H, Beckwith J. 2009. Detecting folding intermediates of a protein as it passes through the bacterial translocation channel. Cell 138:1164–1173.

84. Landeta C, Boyd D, Beckwith J. 2018. Disulfide bond formation in prokaryotes. Nat Microbiol 3:270–280.

85. Katzen F, Beckwith J. 2000. Transmembrane electron transfer by the membrane protein DsbD occurs via a disulfide bond cascade. Cell 103:769–779.

86. Stirnimann CU, Grütter MG, Glockshuber R, Capitani G. 2006. nDsbD: a redox interaction hub in the Escherichia coli periplasm. Cell Mol Life Sci 63:1642–1648.

87. Bushweller JH. 2020. Protein Disulfide Exchange by the Intramembrane Enzymes DsbB, DsbD, and CcdA. J Mol Biol 432:5091–5103.

88. Champion OL, Karlyshev A, Cooper IAM, Ford DC, Wren BW, Duffield M, Oyston PCF, Titball RW. 2011. Yersinia pseudotuberculosis mntH functions in intracellular manganese accumulation, which is essential for virulence and survival in cells expressing functional Nramp1. Microbiology 157:1115–1122.

89. Anderson ES, Paulley JT, Gaines JM, Valderas MW, Martin DW, Menscher E, Brown TD, Burns CS, Roop

RM. 2009. The Manganese Transporter MntH Is a Critical Virulence Determinant for *Brucella abortus* 2308 in Experimentally Infected Mice. Infect Immun 77:3466–3474.

90. Boyer E, Bergevin I, Malo D, Gros P, Cellier MFM. 2002. Acquisition of Mn(II) in addition to Fe(II) is required for full virulence of Salmonella enterica serovar Typhimurium. Infection and Immunity 70:6032–6042.

91. Zaharik ML, Cullen VL, Fung AM, Libby SJ, Kujat Choy SL, Coburn B, Kehres DG, Maguire ME, Fang FC, Finlay BB. 2004. The Salmonella enterica serovar typhimurium divalent cation transport systems MntH and SitABCD are essential for virulence in an Nramp1G169 murine typhoid model. Infect Immun 72:5522–5525.

92. Yu Y, Li Y-P, Ren K, Hao X, Fru EC, Rønn R, Rivera WL, Becker K, Feng R, Yang J, Rensing C. 2024. A brief history of metal recruitment in protozoan predation. Trends Microbiol 32:465–476.

93. Crossman LC, Gould VC, Dow JM, Vernikos GS, Okazaki A, Sebaihia M, Saunders D, Arrowsmith C, Carver T, Peters N, Adlem E, Kerhornou A, Lord A, Murphy L, Seeger K, Squares R, Rutter S, Quail MA, Rajandream MA, Harris D, Churcher C, Bentley SD, Parkhill J, Thomson NR, Avison MB. 2008. The complete genome, comparative and functional analysis of Stenotrophomonas maltophilia reveals an organism heavily shielded by drug resistance determinants. Genome Biol 9:R74.

94. Sendra KM, Barwinska-Sendra A, Mackenzie ES, Baslé A, Kehl-Fie TE, Waldron KJ. 2023. An ancient metalloenzyme evolves through metal preference modulation. Nat Ecol Evol 7:732–744.

95. Martin JE, Imlay JA. 2011. The alternative aerobic ribonucleotide reductase of Escherichia coli, NrdEF, is a manganese-dependent enzyme that enables cell replication during periods of iron starvation. Mol Microbiol 80:319–334.

96. Makhlynets O, Boal AK, Rhodes DV, Kitten T, Rosenzweig AC, Stubbe J. 2014. Streptococcus sanguinis class Ib ribonucleotide reductase: high activity with both iron and manganese cofactors and structural insights. J Biol Chem 289:6259–6272.

97. Sobota JM, Imlay JA. 2011. Iron enzyme ribulose-5-phosphate 3-epimerase in Escherichia coli is rapidly damaged by hydrogen peroxide but can be protected by manganese. Proc Natl Acad Sci U S A 108:5402–5407.

98. Imlay JA. 2014. The mismetallation of enzymes during oxidative stress. J Biol Chem 289:28121–28128.

99. Song M, Kim J-S, Liu L, Husain M, Vázquez-Torres A. 2016. Antioxidant Defense by Thioredoxin Can Occur Independently of Canonical Thiol-Disulfide Oxidoreductase Enzymatic Activity. Cell Rep 14:2901–2911.

100. Uppalapati SR, Vazquez-Torres A. 2022. Manganese Utilization in Salmonella Pathogenesis: Beyond the Canonical Antioxidant Response. Front Cell Dev Biol 10:924925.

101. Hood MI, Skaar EP. 2012. Nutritional immunity: transition metals at the pathogen–host interface. Nat Rev Microbiol 10:525–537.

102. Ouyang A, Gasner KM, Neville SL, McDevitt CA, Frawley ER. 2022. MntP and YiiP Contribute to Manganese Efflux in Salmonella enterica Serovar Typhimurium under Conditions of Manganese Overload and Nitrosative Stress. Microbiol Spectr 10:e01316-21.

103. Ogunniyi AD, Mahdi LK, Jennings MP, McEwan AG, McDevitt CA, Van Der Hoek MB, Bagley CJ, Hoffmann P, Gould KA, Paton JC. 2010. Central Role of Manganese in Regulation of Stress Responses, Physiology, and Metabolism in *Streptococcus pneumoniae*. J Bacteriol 192:4489–4497.

104. Sullivan MJ, Terán I, Goh KGK, Ulett GC. 2024. Resisting death by metal: metabolism and Cu/Zn homeostasis in bacteria. Emerging Topics in Life Sciences 8:45–56.

105. Pi H, Wendel BM, Helmann JD. 2020. Dysregulation of Magnesium Transport Protects Bacillus subtilis against Manganese and Cobalt Intoxication. J Bacteriol 202.

106. Hohle TH, O'Brian MR. 2014. Magnesium-dependent processes are targets of bacterial manganese toxicity. Molecular Microbiology 93:736–747.

107. Osman D, Martini MA, Foster AW, Chen J, Scott AJP, Morton RJ, Steed JW, Lurie-Luke E, Huggins TG, Lawrence AD, Deery E, Warren MJ, Chivers PT, Robinson NJ. 2019. Bacterial sensors define intracellular free energies for correct enzyme metalation. Nat Chem Biol 15:241–249.

108. Irving H, Williams RJP. 1953. 637. The stability of transition-metal complexes. J Chem Soc 3192.

109. Ochoa-Sánchez LE, Vinuesa P. 2017. Evolutionary Genetic Analysis Uncovers Multiple Species with Distinct Habitat Preferences and Antibiotic Resistance Phenotypes in the Stenotrophomonas maltophilia Complex. Front Microbiol 8:1548.

110. LaBauve AE, Wargo MJ. 2012. Growth and laboratory maintenance of Pseudomonas aeruginosa. Curr Protoc Microbiol Chapter 6:Unit 6E.1.

111. Hoang TT, Karkhoff-Schweizer RR, Kutchma AJ, Schweizer HP. 1998. A broad-host-range Flp-FRT recombination system for site-specific excision of chromosomally-located DNA sequences: application for isolation of unmarked Pseudomonas aeruginosa mutants. Gene 212:77–86.

112. Martínez-García E, Fraile S, Algar E, Aparicio T, Velázquez E, Calles B, Tas H, Blázquez B, Martín B, Prieto C, Sánchez-Sampedro L, Nørholm MHH, Volke DC, Wirth NT, Dvořák P, Alejaldre L, Grozinger L, Crowther M, Goñi-Moreno A, Nikel PI, Nogales J, de Lorenzo V. 2023. SEVA 4.0: an update of the Standard European Vector Architecture database for advanced analysis and programming of bacterial phenotypes. Nucleic Acids Research 51:D1558–D1567.

113. Andrews, S. 2010. Fastqc: A quality control tool for high throughput sequence data (v0.11.2). Babraham bioinformatics Institute, Cambridge, UK.

114. Bolger AM, Lohse M, Usadel B. 2014. Trimmomatic: a flexible trimmer for Illumina sequence data. Bioinformatics 30:2114–2120.

115. Langmead B, Salzberg SL. 2012. Fast gapped-read alignment with Bowtie 2. Nat Methods 9:357–359.

116. Liao Y, Smyth GK, Shi W. 2019. The R package Rsubread is easier, faster, cheaper and better for alignment and quantification of RNA sequencing reads. Nucleic Acids Research 47:e47–e47.

117. Love MI, Huber W, Anders S. 2014. Moderated estimation of fold change and dispersion for RNA-seq data with DESeq2. Genome Biol 15:550.

118. The UniProt Consortium. 2017. UniProt: the universal protein knowledgebase. Nucleic Acids Res 45:D158–D169.

119. Blum M, Andreeva A, Florentino LC, Chuguransky SR, Grego T, Hobbs E, Pinto BL, Orr A, Paysan-Lafosse T, Ponamareva I, Salazar GA, Bordin N, Bork P, Bridge A, Colwell L, Gough J, Haft DH, Letunic I, Llinares-López F, Marchler-Bauer A, Meng-Papaxanthos L, Mi H, Natale DA, Orengo CA, Pandurangan AP, Piovesan D, Rivoire C, Sigrist CJA, Thanki N, Thibaud-Nissen F, Thomas PD, Tosatto SCE, Wu CH, Bateman A. 2025. InterPro: the protein sequence classification resource in 2025. Nucleic Acids Research 53:D444–D456.

120. Erill I. 2015. Every Site Counts: Submitting Transcription Factor-Binding Site Information through the CollecTF Portal. J Bacteriol 197:2454–2457.

121. Dudek C-A, Jahn D. 2022. PRODORIC: state-of-the-art database of prokaryotic gene regulation. Nucleic Acids Research 50:D295–D302.

122. Sievers F, Higgins DG. 2018. Clustal Omega for making accurate alignments of many protein sequences. Protein Science 27:135–145.

FIGURE LEGENDS

FIG 1. Growth kinetics of *S. maltophilia* Sm18 under increasing Mn concentration. (A) Growth in Luria-Bertani (LB) and minimal MOPS (MM) media with increasing millimolar (mM) concentrations of manganese (Mn^{2+}). The means of eight biological replicates per concentration are represented by distinct shapes and colors, with error bars indicating the standard error. (B) Statistical analysis of Mn tolerance in Sm18. Differences among groups were assessed using the Kruskal-Wallis test, followed by Dunn's *post hoc* test with Benjamini-Hochberg (BH) correction. Significance levels are shown as:

ns, P > 0.05; *, P < 0.05; **, P < 0.01; ***, P < 0.001; ***, P < 0.0001. Black asterisks indicate comparisons with the manganese-free control, and red asterisks indicate comparisons between other groups.

FIG 2. Transcriptomic analysis and identification of differentially expressed genes (DEGs). (A) Principal component analysis (PCA) based on DESeq2-normalized read counts from the full transcriptome (*n* = 4,059). (B) Venn diagram generated using the VennDiagram package in R, illustrating the overlap of DEGs at different metal concentrations. Genes were considered differentially expressed if they met the criteria of adjusted P-value (padj) < 0.01 and $|\log_2$ fold change$| \geq 1$. (C) DEGs from Mn^{2+} 0 μM vs. Mn^{2+} 8 μM comparisons in MM-Fe10 and MM-Fe0 mapped across the Sm18 chromosome (Chr Sm18). Green loci denote regions with significantly different expression. Colored dots represent genes classified into Gene Ontology (GO) functional categories. The adjacent bar chart displays the InterPro-based annotations of each DEG.

FIG 3. Core components of the MntR miniregulon in *S. maltophilia* Sm18. (A) Binding motif for the transcription factor MntR (MntR-box) identified using MEME. The MntR box corresponds to a 16-bp inverted palindromic sequence. (B) Putative manganese uptake operon encoding an outer membrane TonB-dependent receptor and a thioredoxin-fold protein, identified by locus tags 2357 and 2358, respectively. The MntR-box is located 75 bp upstream of the start codon, between the -10 and -35 promoter regions. These genes are adjacent to *mntR* and *mntH*, which share an 117 bp intergenic region. The *mntH* MntR-box is located 10 bp upstream of the start codon. (C) The gene encoding the inner membrane manganese exporter MntP is predicted to be regulated by both the *yybP-ykoY* riboswitch and MntR. Its MntR-box is located 247 bp upstream of the start codon.

FIG 4. Distribution of the MntR miniregulon proteins across *Stenotrophomonas* species and closely related *Lysobacteraceae* genera (see color codes). Maximum-likelihood core-genome phylogeny estimated with IQ-TREE based on the concatenation of 155 top-scoring protein families selected with GET_PHYLOMARKERS from 103 *Lysobacteraceae* RefSeq genomes. The tree integrates taxonomic information (four inner rings) with the presence/absence patterns of the MntR miniregulon genes (*orf0235*, *orf02358, mntH*, *mntR*, *and mntP*) identified by hmmsearch (five outer rings) and the number of MntR boxes detected by MAST scanning (bars). *S. maltophilia* strains are labeled in bold font, with Sm18 highlighted in yellow. Bipartition support values are given as UFBoot bootstrap percentages only for those ≥ 70%. The scale bar represents the number of expected substitutions per site under the best-fitting Q.insect+F+R4 model, as selected by BIC.

FIG 5 Statistical analysis of fluorescence intensity for transcriptional fusions of Sm18 genes within the

manganese MntR miniregulon. (A) Area under the curve (AUC) of normalized relative fluorescence units (RFU), normalized using the RFU of strains carrying the empty pSEVA-327 plasmid. Nine biological replicates were grown in minimal medium MOPS (MM) supplemented with 30 µg/mL of chloramphenicol. AUC values of the transcriptional fusions Sm18/327-2357_2358, Sm18/327-*mntH*, and Sm18/327-*mntP* are shown as mean ± 95% CI (bootstrap) for 0 and 10 µM Fe^{2+}. Each Fe condition was tested with 0, 0.08, and 8 µM Mn^{2+}. (B) AUC of normalized RFU for five biological and four technical replicates of Sm18 and Sm18ΔmntR strains harboring the same fusions grown in MM-Fe0. Differences were assessed using the Kruskal–Wallis test, followed by Dunn's *post hoc* test with BH correction. Significance levels are shown as: ns, $P > 0.05$; *, $P < 0.05$; **, $P < 0.01$; ***, $P < 0.001$; ***, $P < 0.0001$. Black asterisks denote comparisons across Mn concentrations, red asterisks denote Fe comparisons, and gray asterisks indicate the combined Fe/Mn variations.

FIG 6 Structural and phylogenetic analysis of the novel CQNC family of TBDRs. (A-E) Domain organization and AF3 models of V8P27_002357 showing the β-barrel (teal), plug domain (orange), and residues forming an ionic lock (R19-D332). (F-J) Mn^{2+}-bound AF3 models highlighting coordinating residues (C63, C66, E247, and H446), statistical analysis of donor-metal distances retrieved from the MESPEUS database, and structural effects of ionic lock disruption upon Mn^{2+} binding. (K-L) Maximum-likelihood phylogeny and ESPript alignment showing the conserved CQNC motif characteristic of the CQNC-TBDR family.

FIG 7 Comparative genomics of the TBDR-pTFP locus and structural features of the thioredoxin-fold protein (pTFP) V8P27_002358. (A) Multiple alignment showing conserved synteny of TBDR-pTFP loci across Lysobacterales, Sphingomonadales, and Opitutales. Gray shading indicates sequence identities. Loci were ordered according to a neighbor-joining tree based on the Mash distances. (B-C) AF3 models and 2D cartoon of V8P27_002358 showing canonical thioredoxin-fold organization (light blue and ruby units), oxidized CXXC motif (C39-C42), and a secondary disulfide bridge (C147-C154). (D-E) Structure-guided multiple-sequence alignment of CQNC-TBDRs and a close-up of the CXXC motif showing residues predicted to form hydrogen bonds with catalytic cysteines (C39, C42).

FIG 8. Phenotypic characterization of *mntH* and *mntP* mutants of *S. maltophilia* Sm18. (A-B) Growth kinetics of the Sm18VIM-*mntH* mutant under oxidative stress induced by hydrogen peroxide (H_2O_2) at different pH values. The *mntH* mutant showed no growth defects under Fe^{2+}- or Mn^{2+}-limiting conditions but exhibited increased sensitivity to hydrogen peroxide (0.2 and 0.5 mM), particularly at neutral pH (orange triangles). (C-D) Growth kinetics of the markerless Sm18Δ*mntP* mutant exposed to increasing Mn^{2+} concentrations (5-160 µM). Deletion of *mntP* resulted in significant manganese sensitivity starting at 40 µM, with complete growth inhibition at higher concentrations.

Complementation with the plasmid pSEVA332 carrying *mntH* or *mntP* under their native promoters restored the wild-type phenotype (green cubes). Error bars represent the SEM for growth kinetics and 95% CI (bootstrap) for AUC analysis of three biological replicates. Statistical significance was evaluated using the Kruskal–Wallis test with Dunn's *post hoc* BH correction: ns, $P > 0.05$; *, $P < 0.05$; **, $P < 0.01$; ***, $P < 0.001$; and ****, $P < 0.0001$. Blue asterisks denote comparisons between wild type (blue circles) and mutants; orange asterisks indicate comparisons across H_2O_2 or Mn^{2+} concentrations.

FIG 9. Live-cell imaging of Sm18/337-*mntH* promoter activity and intracellular replication of the Sm18VIM-*mntH* mutant in co-culture with *Acanthamoeba castellanii* trophozoites. (A) Representative images from six biological replicates of Sm18/337R−*mntH* and *A. castellanii* co-cultures at 3 and 18 h after primary contact. Promoter activity was visualized in the red channel (mCherry2). Trophozoites were imaged using brightfield microscopy. (B) Fluorescence kinetics of mScarlet-I-labeled strains: Sm18 (blue triangles), Sm18VIM*mntH* (orange cubes), and Sm18Δ*mntR* (green lines). Background fluorescence from medium-bacteria controls was subtracted for the normalization. (C) Kruskal–Wallis test was used to compare the medians between groups. When significant differences were detected, pairwise comparisons were performed using Dunn's test with a Bonferroni correction. Significance levels: ns, $P > 0.05$; *, $P < 0.05$; **, $P < 0.01$; ***, $P < 0.001$; ****, $P < 0.0001$.

FIG10. Integrative model of the MntR miniregulon in *Stenotrophomonas maltophilia*. (A) Schematic representation of the canonical MntR-dependent system regulating manganese homeostasis through the complementary functions of the cytoplasmic membrane transporters MntH and MntP. MntH mediates Mn^{2+} uptake under metal limitation, whereas MntP facilitates its efflux under overload. (B) Overview of the additional components. A novel bicistronic operon encodes a TonB-dependent outer membrane receptor (CQNC-TBDR, V8P27_02357) and a thioredoxin-fold periplasmic protein (pTFP, V8P27_02358), whose expression is strongly induced under Mn and Fe limitation and is only partially dependent on MntR. Synteny and coexpression suggest that both proteins form a coupled system for manganese acquisition, with pTFP acting as a putative periplasmic dithiol reductase of the preceding CQNC-TBDR. Other transporters, including CDF and RND efflux pumps, also exhibited differential expression under these conditions but were not further analyzed in this study. (C) Model of the intracellular environment during bacterial internalization by professional phagocytes. *S. maltophilia* experiences Mn and Fe restriction within the phagosome, although it may not be strong enough during the first 18 h to trigger TBDR gene expression. In contrast, *mntH* is highly expressed and required for optimal intracellular replication in *A. castellanii* trophozoites. These findings support the role of MntH in counteracting host-imposed Mn (and possibly Fe) limitations and maintaining metal homeostasis under oxidative stress conditions. Created with https://BioRender.com.

SUPPLEMENTAL DATA

Supplemental data are available from https://github.com/vinuesa/supplementary_materials/tree/main/docs/Argueta-Zepeda_Stenotrophomonas_MntR_miniregulon.

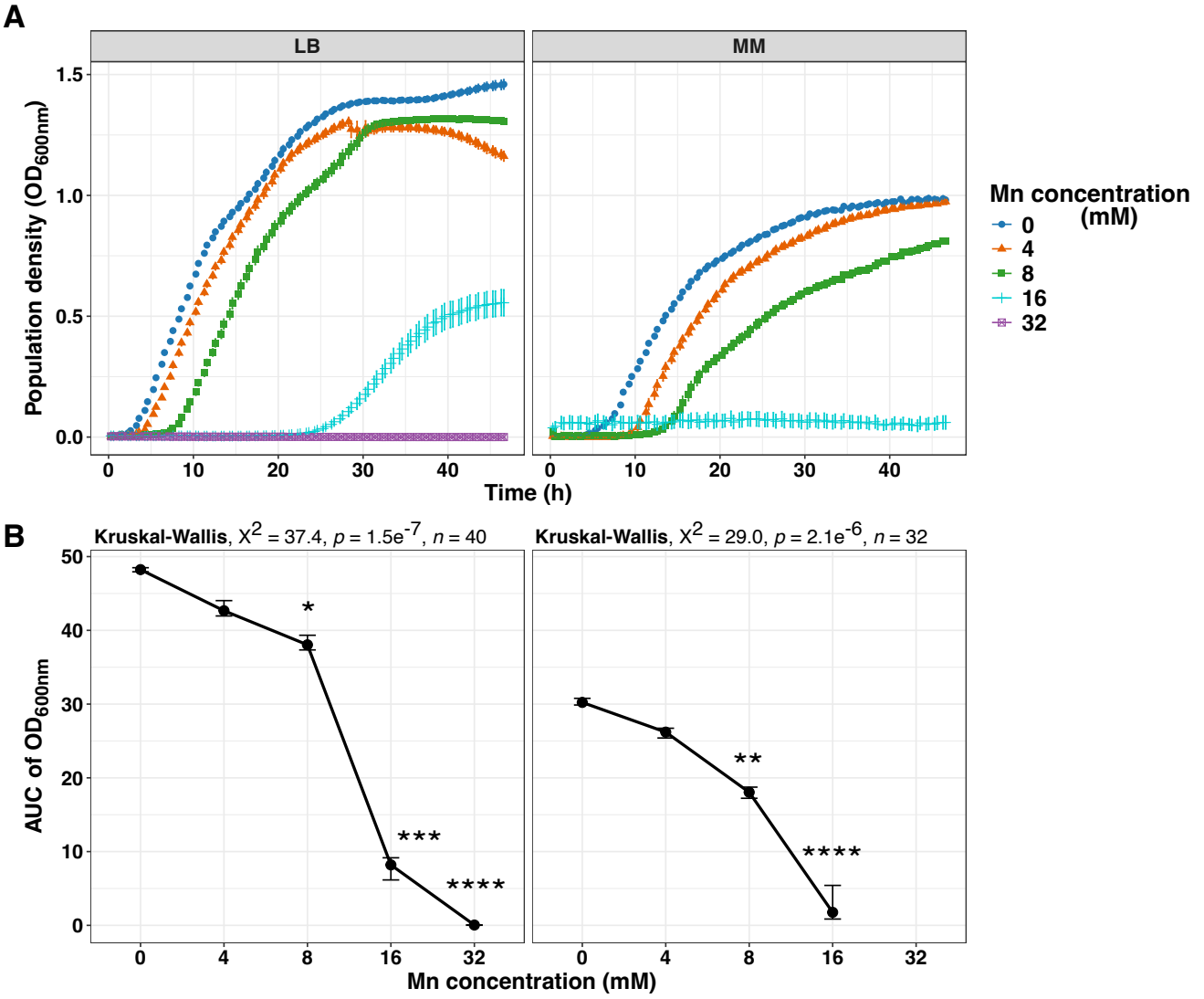

Evaluated contrasts

group1	group2	p.adj	p.adj.signif
0	8	1.101202e−02	*
0	16	1.470991e−04	***
0	32	4.379815e−07	****
4	16	1.101202e−02	*
4	32	1.470991e−04	***
8	32	1.101202e−02	*

group1	group2	p.adj	p.adj.signif
0	8	1.293498e−03	**
0	16	1.864407e−06	****
4	16	1.293498e−03	**

pwc: **Dunn test**; p.adjust: **Benjamini-Hochberg**

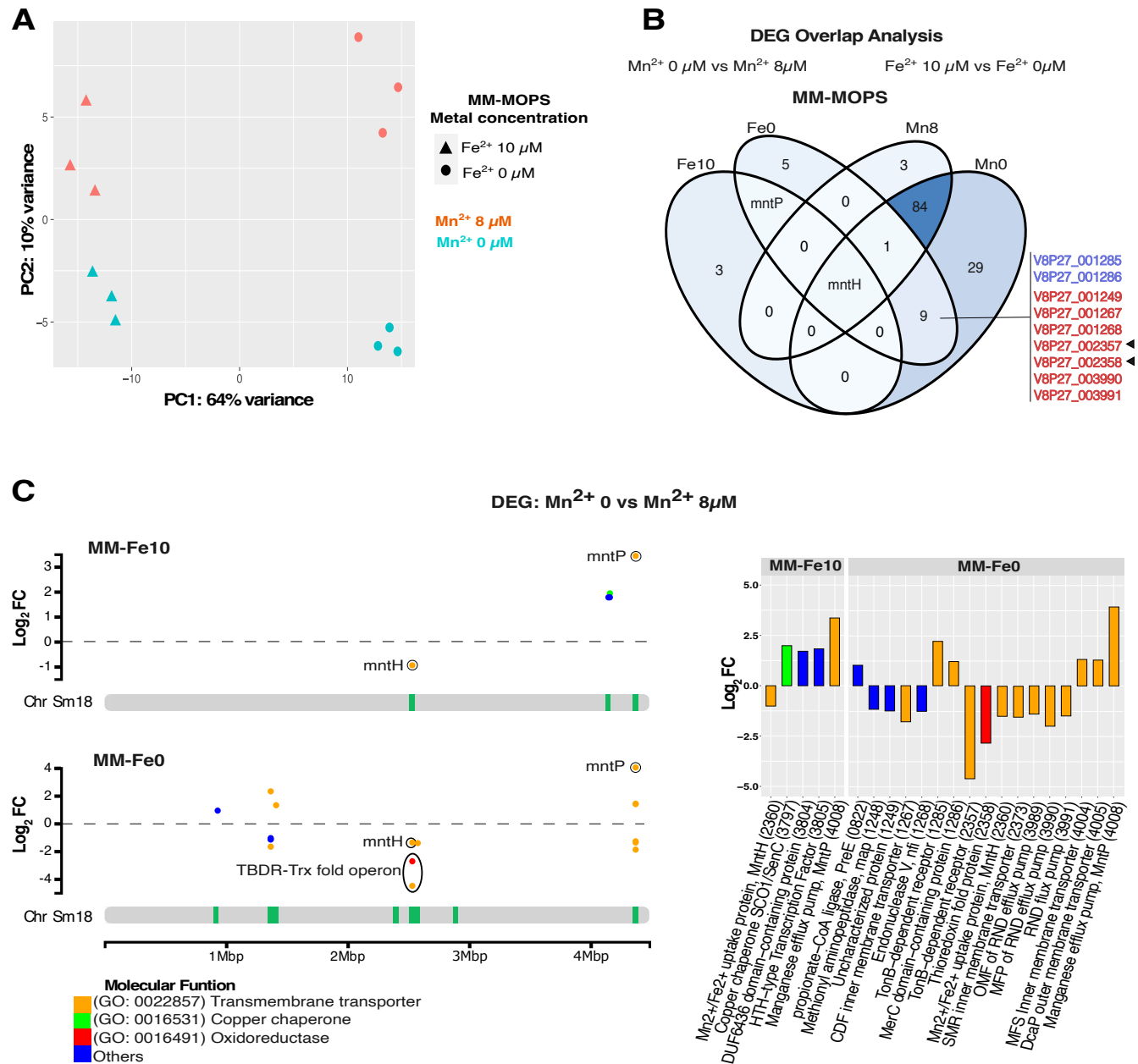
A
PC2: 10% variance
PC1: 64% variance
MM-MOPS
Metal concentration
Fe2+ 10 μM
Fe2+ 0 μM
Mn2+ 8 μM
Mn2+ 0 μM
B
DEG Overlap Analysis
Mn2+ 0 μM vs Mn2+ 8μM
Fe2+ 10 μM vs Fe2+ 0μM
MM-MOPS
Fe10
Fe0
Mn8
Mn0
mntP
mntH
V8P27_001285
V8P27_001286
V8P27_001249
V8P27_001267
V8P27_001268
V8P27_002357
V8P27_002358
V8P27_003990
V8P27_003991
C
DEG: Mn2+ 0 vs Mn2+ 8μM
MM-Fe10
MM-Fe0
Log2FC
mntP
mntH
Chr Sm18
TBDR-Trx fold operon
1Mbp
2Mbp
3Mbp
4Mbp
Molecular Funtion
(GO: 0022857) Transmembrane transporter
(GO: 0016531) Copper chaperone
(GO: 0016491) Oxidoreductase
Others
Mn2+/Fe2+ uptake protein, MntH (2360)
Copper chaperone SCO1/SenC (3797)
DUF6436 domain-containing protein (3804)
HTH-type Transcription Factor (3805)
Manganese efflux pump, MntP (4008)
propionate-CoA ligase, PreE (0822)
Methionyl aminopeptidase, map (1248)
Uncharacterized protein (1249)
CDF inner membrane transporter (1267)
Endonuclease V, nfi (1268)
TonB-dependent receptor (1285)
TonB-containing protein (1286)
MerC domain-containing protein (2357)
Thioredoxin fold protein (2358)
Mn2+/Fe2+ uptake protein, MntH (2360)
SMR inner membrane transporter (2373)
OMF of RND efflux pump (3989)
MFP of RND efflux pump (3990)
RND flux pump (3991)
MFS Inner membrane transporter (4004)
DcaP outer membrane transporter (4005)
Manganese efflux pump, MntP (4008)

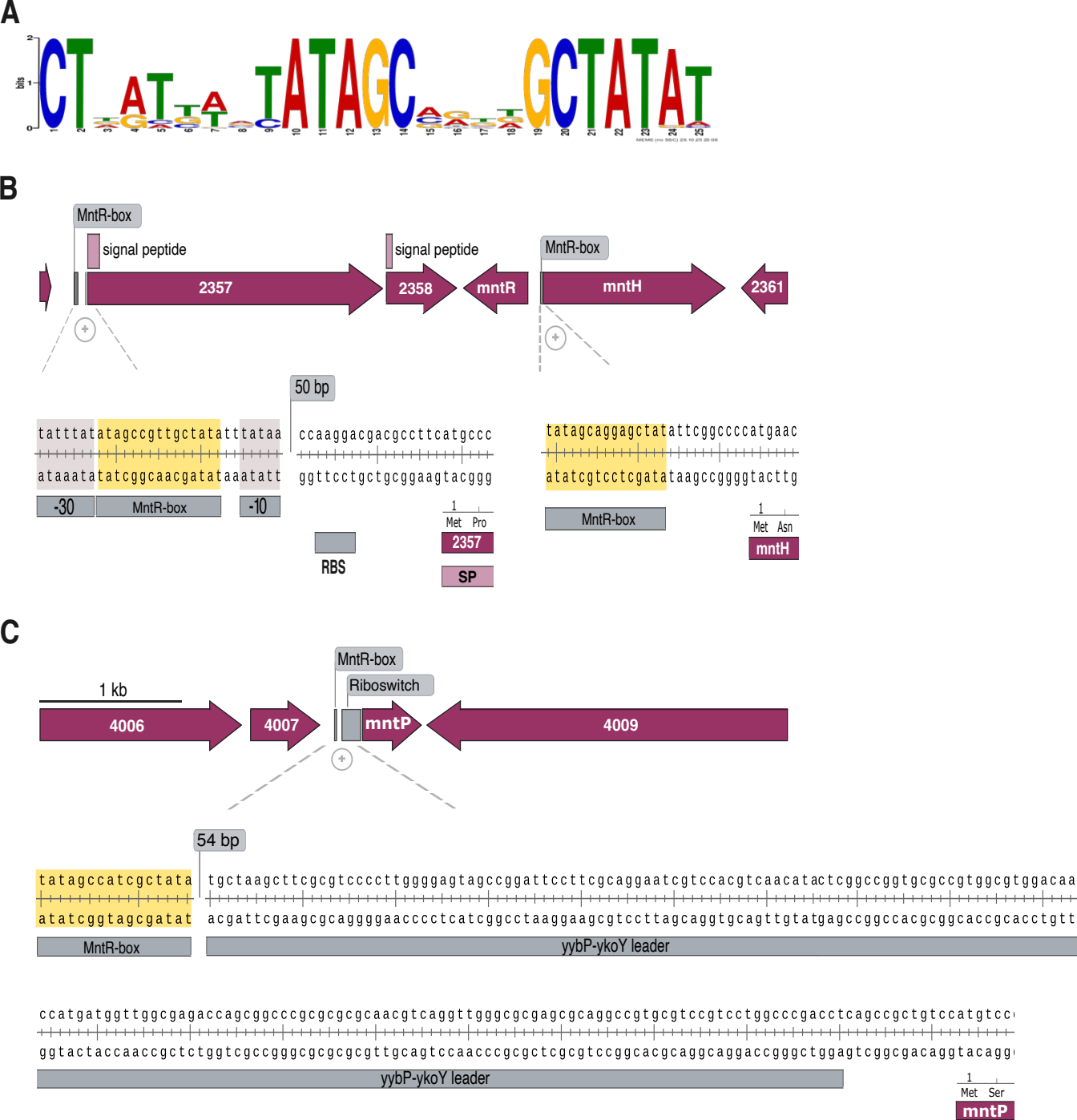
A
bits
B
MntR-box
signal peptide
2357
signal peptide
2358
mntR
MntR-box
mntH
2361
50 bp
tatttatatagccgttgctatatttataa
ataaatatatcggcaacgatataaatatt
ccaaggacgacgccttcatgccc
ggttcctgctgcggaagtacggg
tatagcaggagctatattcggccccatgaac
atatcgtcctcgatataagccggggtacttg
-30
MntR-box
-10
RBS
Met Pro
2357
SP
MntR-box
Met Asn
mntH
C
1 kb
4006
4007
MntR-box
Riboswitch
mntP
4009
54 bp
tatagccatcgctata
atatcggtagcgatat
tgctaagcttcgcgtccccttggggagtagccggattccttcgcaggaatcgtccacgtcaacatactcggccggtgcgccgtggcgtggacaa
acgattcgaagcgcaggggaacccctcatcggcctaaggaagcgtccttagcaggtgcagttgtatgagccggccacgcggcaccgcacctgtt
MntR-box
yybP-ykoY leader
ccatgatggttggcgagaccagcggcccgcgcgcgcaacgtcaggttgggcgcgagcgcaggccgtgcgtccgtcctggcccgacctcagccgctgtccatgtcc
ggtactaccaaccgctctggtcgccgggcgcgcgcgttgcagtccaacccgcgctcgcgtccggcacgcaggcaggaccgggctggagtcggcgacaggtacagg
yybP-ykoY leader
Met Ser
mntP

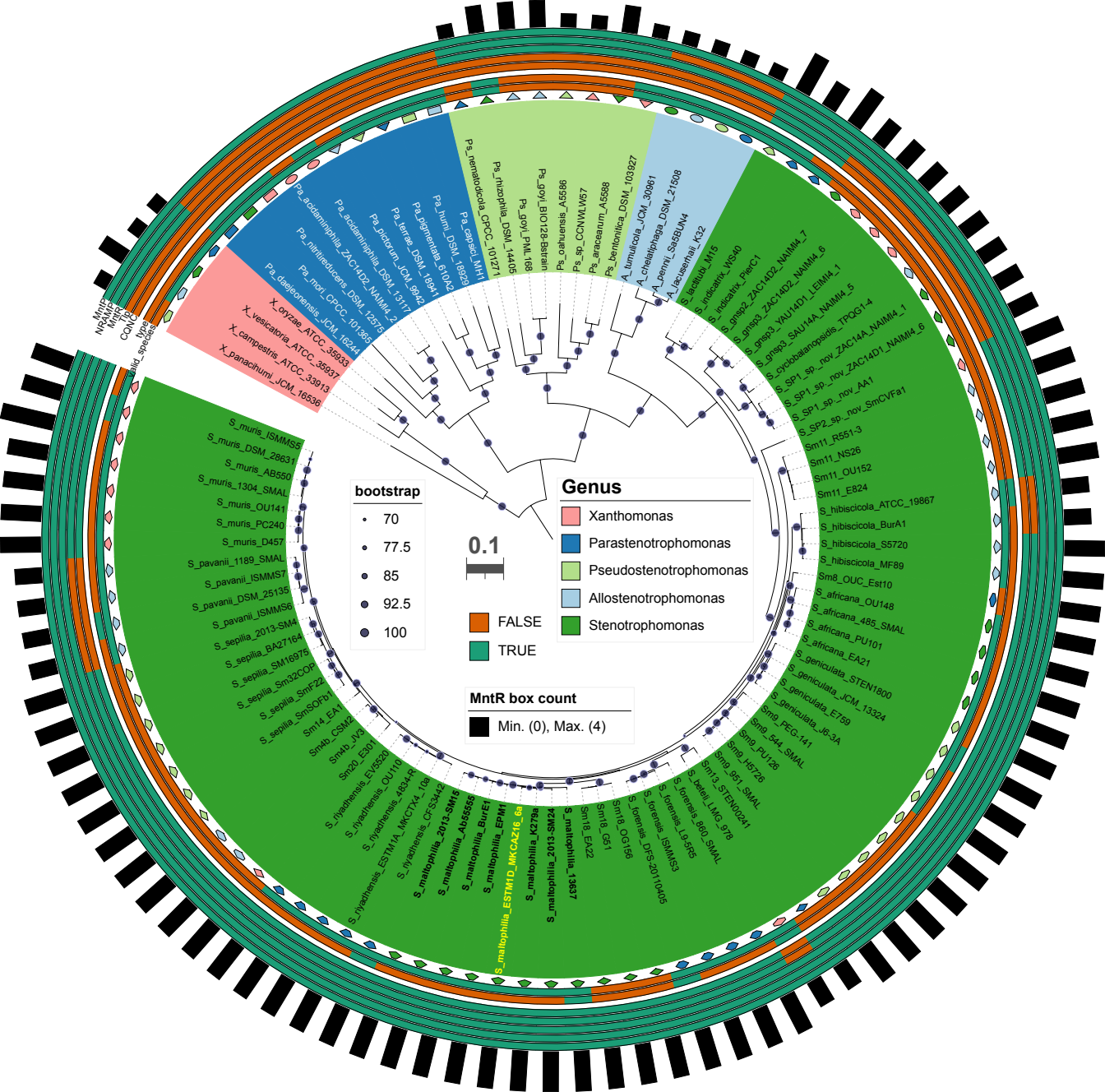
MntR
NRAMP
MntH
CONC
type
valid_species
Pa_nematodicola_CPCC_101271
Pa_rhizophila_DSM_14405
Pa_goyi_PML168
Pa_goyi_CIB128-Serratia
Ps_oahuensis_A5586
Ps_sp._CCNWLW57
Ps_araceanum_A5588
Ps_benitonilica_DSM_103927
A_tumulicola_JCM_30961
A_chelatiphaga_DSM_21508
A_pennyi_Sa5BUN4
A_lacuserhalli_K32
Pa_carpsoli_MH1
Pa_humi_DSM_18929
Pa_pigmentata_610A2
Pa_terrae_DSM_19941
Pa_pictorum_JCM_9942
Pa_acidaminiphila_DSM_13117
Pa_acidaminiphila_ZAC14D2_NAIMI4_2
Pa_mitrifaciens_DSM_12375
Pa_mori_CPCC_101365
Pa_daejeonensis_JCM_16244
X_oryzae_ATCC_35933
X_vesicatoria_ATCC_35937
X_campestris_ATCC_33913
X_panacihumi_JCM_16536
S_lactucae_M15
S_indicatrix_WS40
S_indicatrix_PierC1
S_gnsp2_ZAC14D2_NAIMI4_7
S_gnsp2_ZAC14D2_NAIMI4_6
S_gnsp3_YAU14D1_LEIMI4_1
S_gnsp3_SAU14A_NAIMI4_5
S_cyclobalanopsidis_TPQG1-4
S_SP1_sp._nov_ZAC14A_NAIMI4_1
S_SP1_sp._nov_ZAC14D1_NAIMI4_6
S_SP1_sp._nov_AA1
S_SP2_sp._nov_SmCVFa1
S_SP2_sp._nov_R551-3
Sm11_NS26
Sm11_OU152
Sm11_E824
S_hibiscicola_ATCC_19867
S_hibiscicola_BurA1
S_hibiscicola_S5720
S_hibiscicola_MF89
Sm8_OUC_Est10
S_africana_OU148
S_africana_485_SMAL
S_africana_PU101
S_africana_EA21
S_geniculata_STEN1800
S_geniculata_JCM_13324
S_geniculata_E759
S_geniculata_J6-3A
Sm9_PEG-141
Sm9_544_SMAL
Sm9_PU126
Sm9_H5726
Sm9_951_SMAL
Sm13_STEN00241
S_petalii_LMG_978
S_forensis_860_SMAL
S_forensis_L9-5F5
S_forensis_ISMMS3
S_forensis_DFS_20110405
Sm18_OG156
Sm18_G51
Sm18_EA22
S_maltophilia_13637
S_maltophilia_K279a
S_maltophilia_2013-SM24
S_maltophilia_ESTM1D_MKCAZ16_6a
S_maltophilia_EPM1
S_maltophilia_BurE1
S_maltophilia_Ab555555
S_maltophilia_2013-SM15
S_maltophilia_CFS3442
S_niyadhensis_109
S_niyadhensis_4834-R
S_niyadhensis_OU110
S_niyadhensis_ESTM1A_MKCTX4
S_niyadhensis_EV5520
Sm20_ES01
Sm4b_JK6
Sm14_EA1
Sm4b_CSM2
S_sepilia_SmSOFb1
S_sepilia_SmFZ2
S_sepilia_Sm32COF
S_sepilia_SM16975
S_sepilia_BA27164
S_sepilia_2013-SM4
S_pavanii_DSM_25135
S_pavanii_ISMMS6
S_pavanii_ISMMS7
S_pavanii_1189_SMAL
S_muris_D457
S_muris_PC240
S_muris_OU141
S_muris_1304_SMAL
S_muris_AB550
S_muris_DSM_28631
S_muris_ISMMS5
bootstrap
70
77.5
85
92.5
100
0.1
Genus
Xanthomonas
Parastenotrophomonas
Pseudostenotrophomonas
Allostenotrophomonas
Stenotrophomonas
FALSE
TRUE
MntR box count
Min. (0), Max. (4)

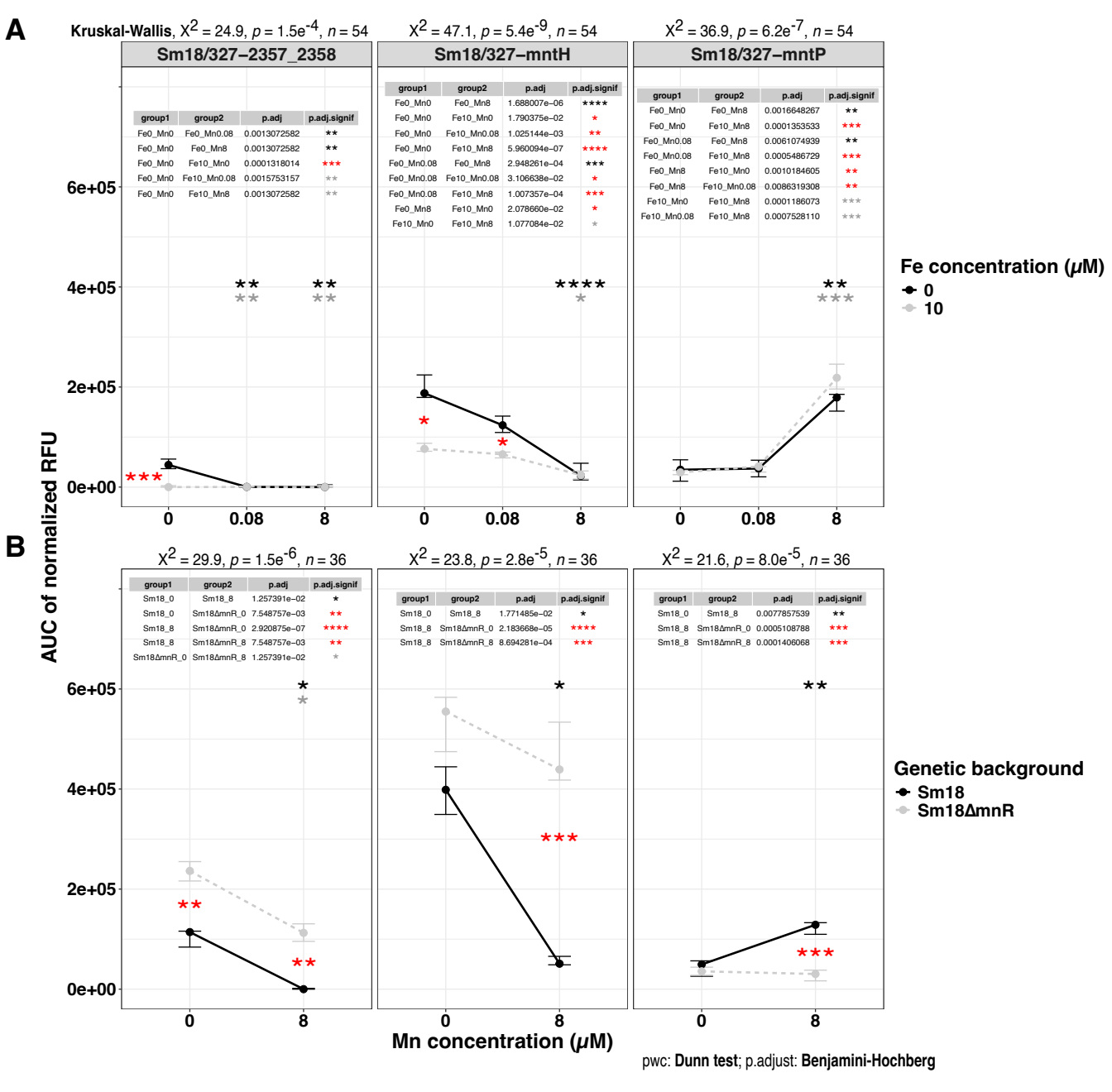
A
Kruskal-Wallis, X^2 = 24.9, p = 1.5e^{-4}, n = 54
X^2 = 47.1, p = 5.4e^{-9}, n = 54
X^2 = 36.9, p = 6.2e^{-7}, n = 54
Sm18/327−2357_2358
Sm18/327−mntH
Sm18/327−mntP
group1 group2 p.adj p.adj.signif
Fe0_Mn0 Fe0_Mn0.08 0.0013072582 **
Fe0_Mn0 Fe0_Mn8 0.0013072582 **
Fe0_Mn0 Fe10_Mn0 0.0001318014 ***
Fe0_Mn0 Fe10_Mn0.08 0.0015753157 **
Fe0_Mn0 Fe10_Mn8 0.0013072582 **
group1 group2 p.adj p.adj.signif
Fe0_Mn0 Fe0_Mn8 1.688007e−06 ****
Fe0_Mn0 Fe10_Mn0 1.790375e−02 *
Fe0_Mn0 Fe10_Mn0.08 1.025144e−03 **
Fe0_Mn0 Fe10_Mn8 5.960094e−07 ****
Fe0_Mn0.08 Fe0_Mn8 2.948261e−04 ***
Fe0_Mn0.08 Fe10_Mn0.08 3.106638e−02 *
Fe0_Mn0.08 Fe10_Mn8 1.007357e−04 ***
Fe0_Mn8 Fe10_Mn0 2.078660e−02 *
Fe10_Mn0 Fe10_Mn8 1.077084e−02 *
group1 group2 p.adj p.adj.signif
Fe0_Mn0 Fe0_Mn8 0.0016648267 **
Fe0_Mn0 Fe10_Mn8 0.0001353533 ***
Fe0_Mn0.08 Fe0_Mn8 0.0061074939 **
Fe0_Mn0.08 Fe10_Mn8 0.0005486729 ***
Fe0_Mn8 Fe10_Mn0 0.0010184605 **
Fe0_Mn8 Fe10_Mn0.08 0.0086319308 **
Fe10_Mn0 Fe10_Mn8 0.0001186073 ***
Fe10_Mn0.08 Fe10_Mn8 0.0007528110 ***
Fe concentration (μM)
0
10
B
X^2 = 29.9, p = 1.5e^{-6}, n = 36
X^2 = 23.8, p = 2.8e^{-5}, n = 36
X^2 = 21.6, p = 8.0e^{-5}, n = 36
group1 group2 p.adj p.adj.signif
Sm18_0 Sm18_8 1.257391e−02 *
Sm18_0 Sm18ΔmnR_0 7.548757e−03 **
Sm18_8 Sm18ΔmnR_0 2.920875e−07 ****
Sm18_8 Sm18ΔmnR_8 7.548757e−03 **
Sm18ΔmnR_0 Sm18ΔmnR_8 1.257391e−02 *
group1 group2 p.adj p.adj.signif
Sm18_0 Sm18_8 1.771485e−02 *
Sm18_8 Sm18ΔmnR_0 2.183668e−05 ****
Sm18_8 Sm18ΔmnR_8 8.694281e−04 ***
group1 group2 p.adj p.adj.signif
Sm18_0 Sm18_8 0.0077857539 **
Sm18_8 Sm18ΔmnR_0 0.0005108788 ***
Sm18_8 Sm18ΔmnR_8 0.0001406068 ***
AUC of normalized RFU
6e+05
4e+05
2e+05
0e+00
0
0.08
8
Mn concentration (μM)
Genetic background
Sm18
Sm18ΔmnR
pwc: Dunn test; p.adjust: Benjamini-Hochberg

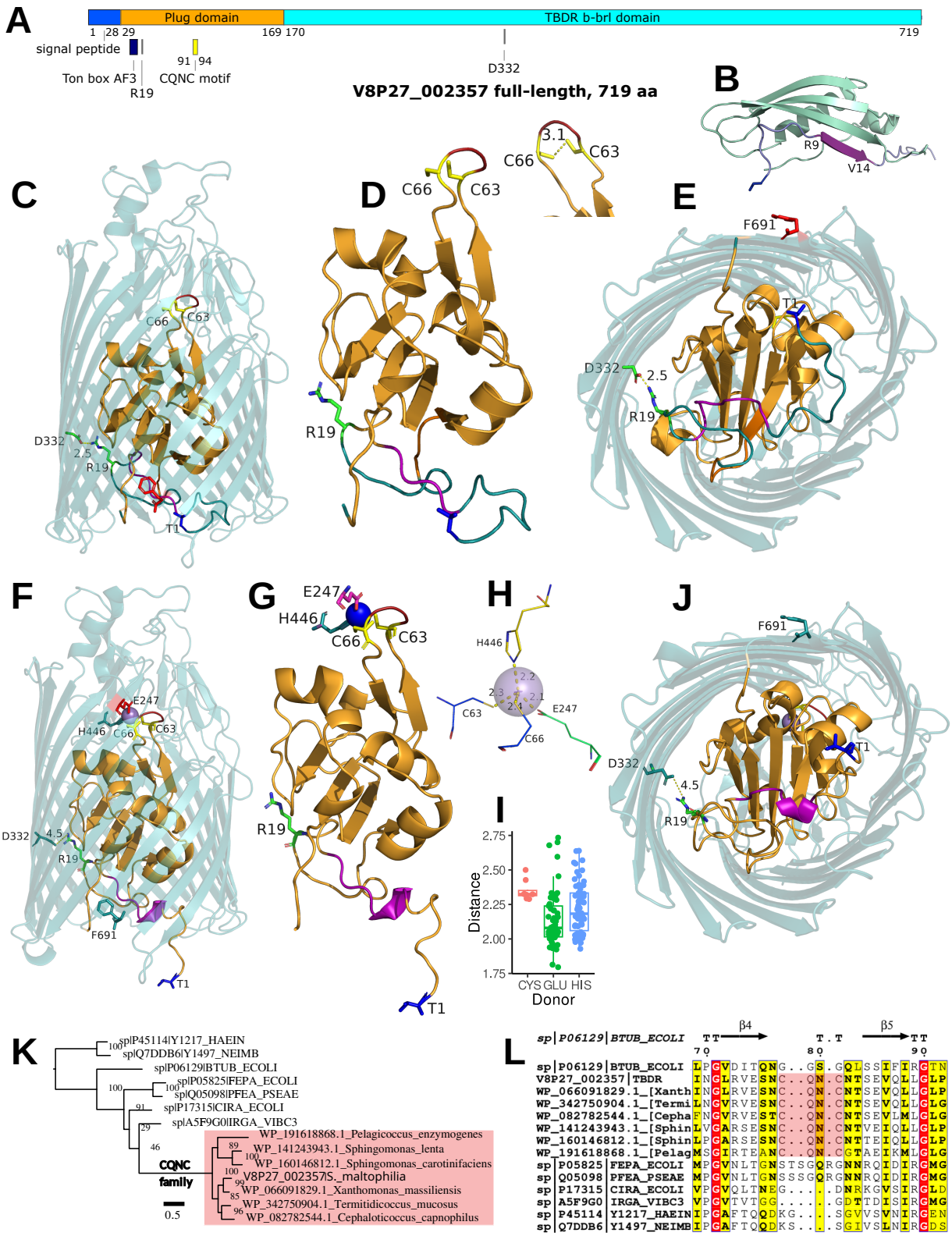
A
Plug domain
TBDR b-brl domain
1 28 29
169 170
719
signal peptide
91 94
Ton box AF3
CQNC motif
R19
D332
V8P27_002357 full-length, 719 aa
B
R9
V14
C
C66
C63
D332
2.5
R19
T1
D
C66
C63
3.1
R19
E
F691
T1
D332
2.5
R19
F
E247
H446
C66
C63
D332
4.5
R19
F691
T1
G
E247
H446
C66
C63
R19
T1
H
H446
C63
E247
C66
D332
I
Distance
CYS GLU HIS
Donor
J
F691
T1
D332
4.5
R19
K
sp|P45114|Y1217_HAEIN
sp|Q7DDB6|Y1497_NEIMB
sp|P06129|BTUB_ECOLI
sp|P05825|FEPA_ECOLI
sp|Q05098|PFEA_PSEAE
sp|P17315|CIRA_ECOLI
sp|A5F9G0|IRGA_VIBC3
WP_191618868.1_Pelagicoccus_enzymogenes
WP_141243943.1_Sphingomonas_lenta
WP_160146812.1_Sphingomonas_carotinifaciens
V8P27_002357|S._maltophilia
WP_066091829.1_Xanthomonas_massiliensis
WP_342750904.1_Termitidicoccus_mucosus
WP_082782544.1_Cephaloticoccus_capnophilus
CQNC family
0.5
L
β4
β5
sp|P06129|BTUB_ECOLI
V8P27_002357|TBDR
WP_066091829.1_[Xanth
WP_342750904.1_[Termi
WP_082782544.1_[Cepha
WP_141243943.1_[Sphin
WP_160146812.1_[Sphin
WP_191618868.1_[Pelag
sp|P05825|FEPA_ECOLI
sp|Q05098|PFEA_PSEAE
sp|P17315|CIRA_ECOLI
sp|A5F9G0|IRGA_VIBC3
sp|P45114|Y1217_HAEIN
sp|Q7DDB6|Y1497_NEIMB

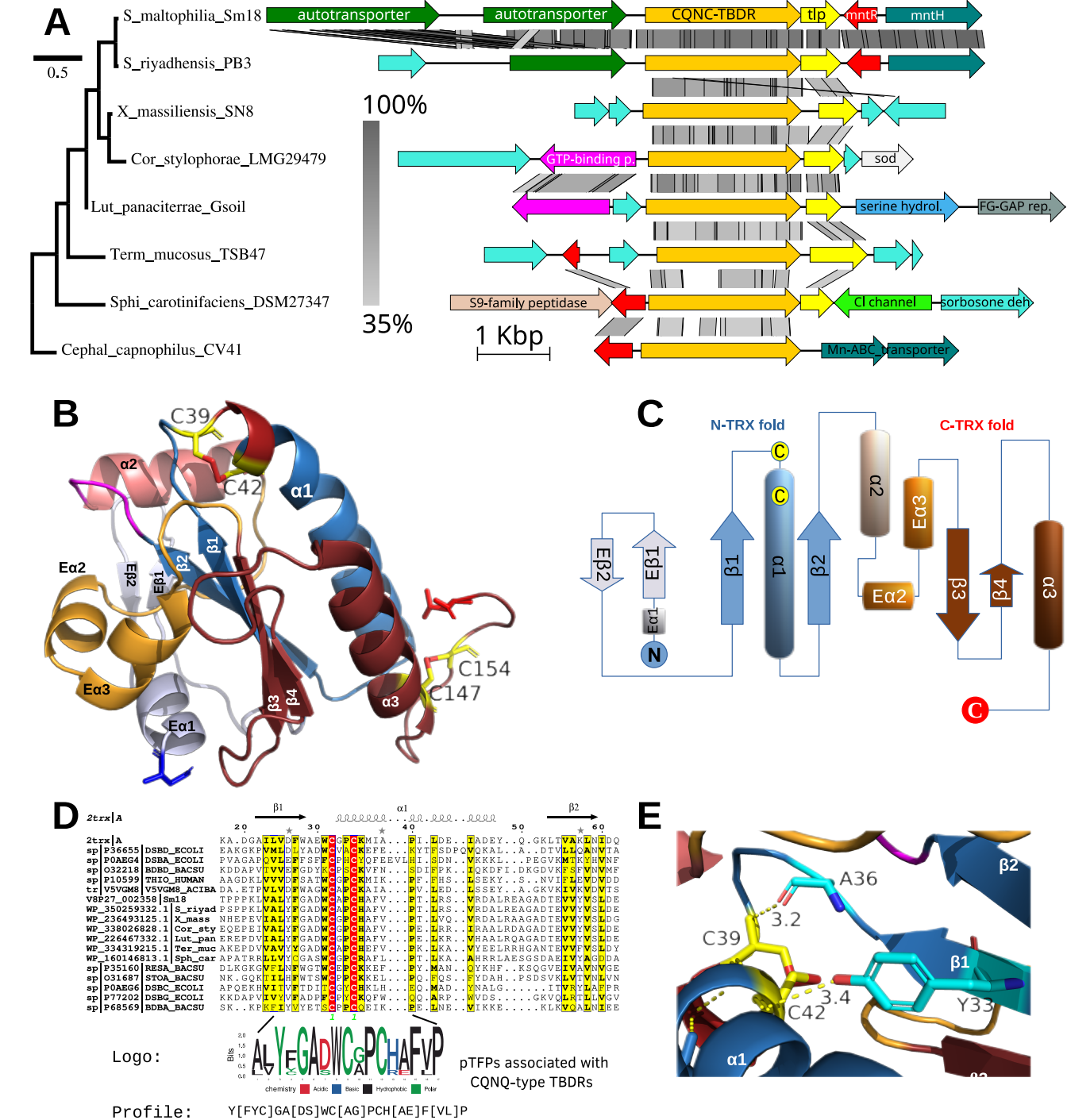
A
0.5
S_maltophilia_Sm18
S_riyadhensis_PB3
X_massiliensis_SN8
Cor_stylophorae_LMG29479
Lut_panaciterrae_Gsoil
Term_mucosus_TSB47
Sphi_carotinifaciens_DSM27347
Cephal_capnophilus_CV41
autotransporter
autotransporter
CQNC-TBDR
tlp
mntR
mntH
100%
35%
GTP-binding p.
sod
serine hydrol.
FG-GAP rep.
S9-family peptidase
Cl channel
sorbosone deh
1 Kbp
Mn-ABC transporter
B
C39
C42
α2
α1
β1
β2
Eα2
Eβ2
Eβ1
Eα3
Eα1
β3
β4
α3
C154
C147
C
N-TRX fold
C-TRX fold
Eβ2
Eβ1
Eα1
N
β1
α1
β2
α2
Eα3
Eα2
β3
β4
α3
C
D
2trx|A
β1
α1
β2
Logo:
Profile:
Y[FYC]GA[DS]WC[AG]PCH[AE]F[VL]P
pTFPs associated with
CQNQ-type TBDRs
E
A36
3.2
C39
3.4
C42
β2
β1
Y33
α1

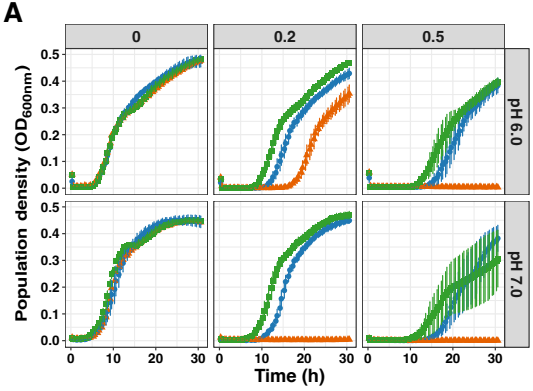
A
0
0.2
0.5
pH 6.0
pH 7.0
Population density (OD600nm)
Time (h)

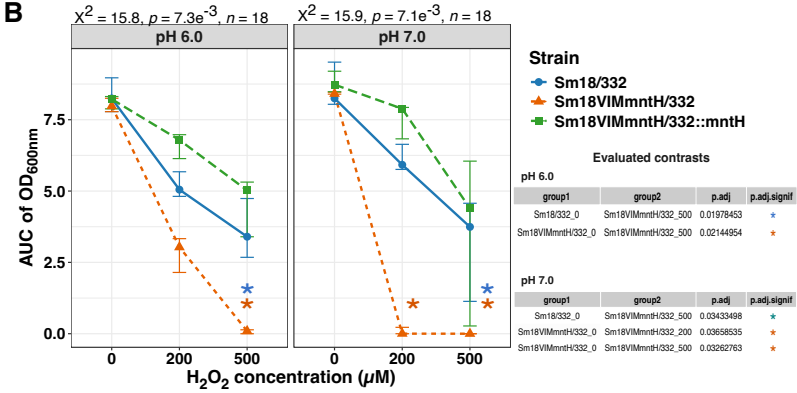
B
X2 = 15.8, p = 7.3e-3, n = 18
X2 = 15.9, p = 7.1e-3, n = 18
pH 6.0
pH 7.0
AUC of OD600nm
H2O2 concentration (μM)
Strain
Sm18/332
Sm18VIMmntH/332
Sm18VIMmntH/332::mntH
Evaluated contrasts
pH 6.0
group1 group2 p.adj p.adj.signif
Sm18/332_0 Sm18VIMmntH/332_500 0.01978453 *
Sm18VIMmntH/332_0 Sm18VIMmntH/332_500 0.02144954 *
pH 7.0
group1 group2 p.adj p.adj.signif
Sm18/332_0 Sm18VIMmntH/332_500 0.03433498 *
Sm18VIMmntH/332_0 Sm18VIMmntH/332_200 0.03658535 *
Sm18VIMmntH/332_0 Sm18VIMmntH/332_500 0.03262763 *

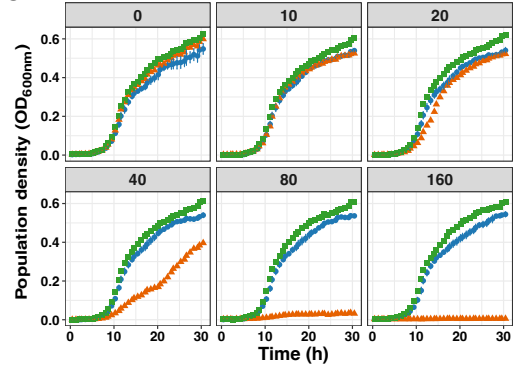
C
0
10
20
40
80
160
Population density (OD600nm)
Time (h)

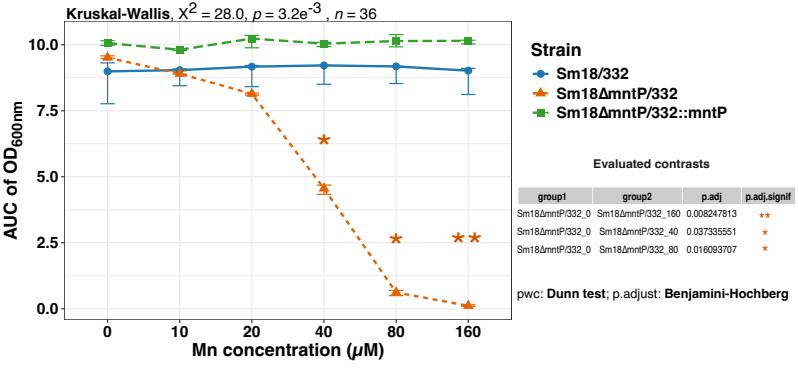
D
Kruskal-Wallis, X2 = 28.0, p = 3.2e-3, n = 36
AUC of OD600nm
Mn concentration (μM)
Strain
Sm18/332
Sm18ΔmntP/332
Sm18ΔmntP/332::mntP
Evaluated contrasts
group1 group2 p.adj p.adj.signif
Sm18ΔmntP/332_0 Sm18ΔmntP/332_160 0.008247813 **
Sm18ΔmntP/332_0 Sm18ΔmntP/332_40 0.037335551 *
Sm18ΔmntP/332_0 Sm18ΔmntP/332_80 0.016093707 *
pwc: Dunn test; p.adjust: Benjamini-Hochberg

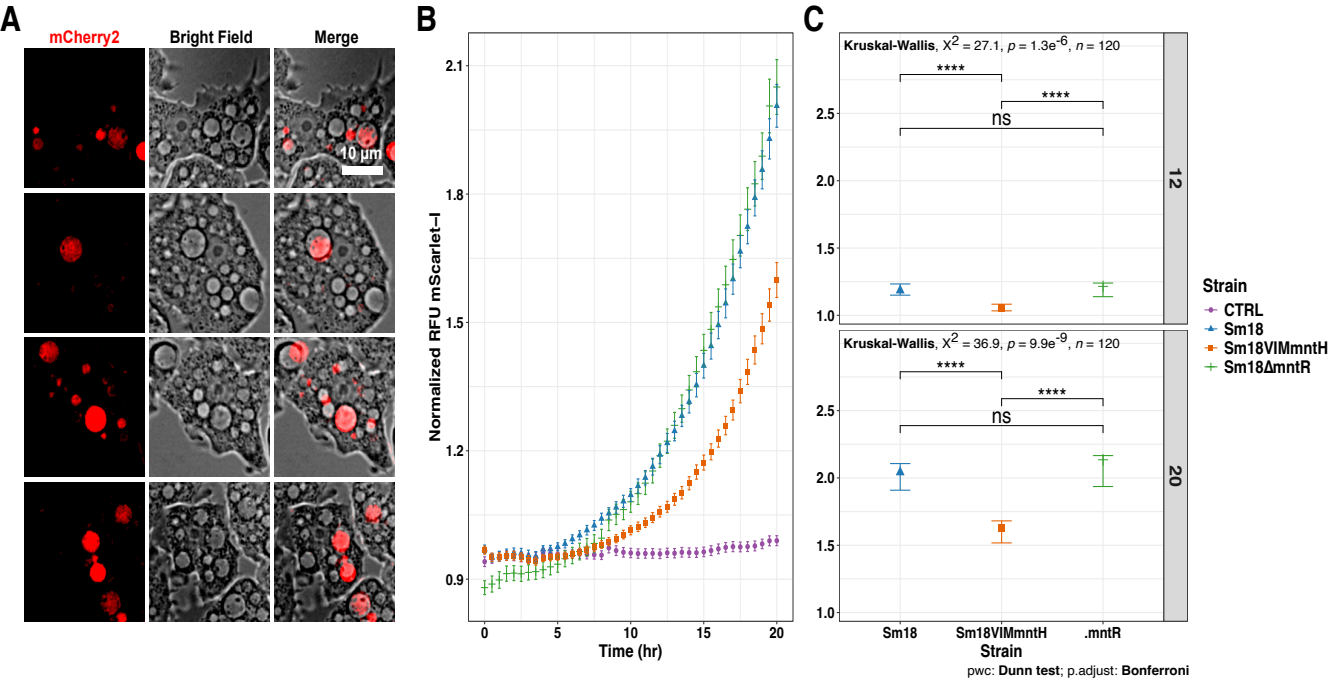
A
mCherry2
Bright Field
Merge
10 µm
B
Normalized RFU mScarlet−I
Time (hr)
C
Kruskal-Wallis, X2 = 27.1, p = 1.3e-6, n = 120
Kruskal-Wallis, X2 = 36.9, p = 9.9e-9, n = 120
****
ns
12
20
Sm18
Sm18VIMmntH
.mntR
Strain
pwc: Dunn test; p.adjust: Bonferroni
Strain
CTRL
Sm18
Sm18VIMmntH
Sm18ΔmntR

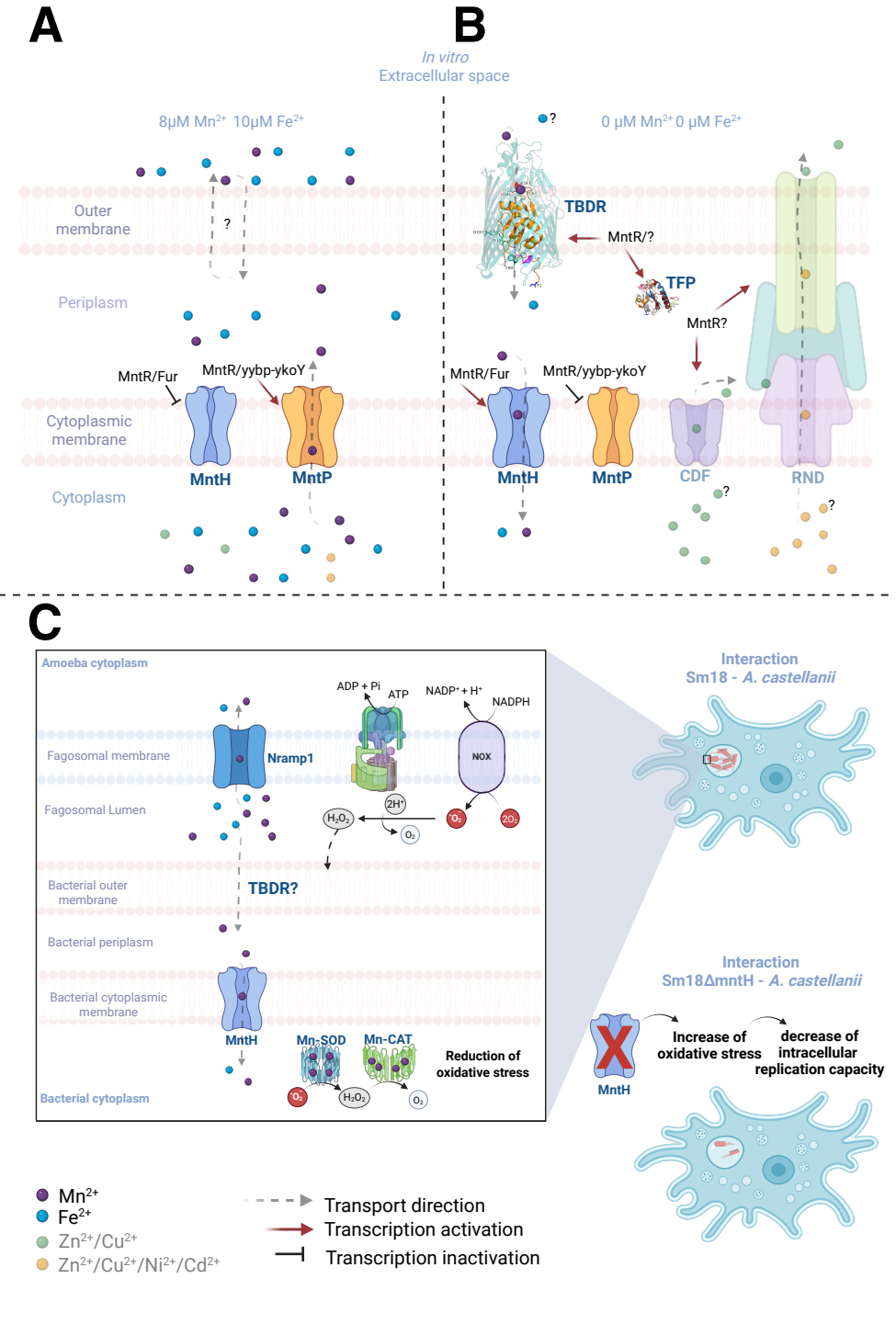
A
8μM Mn2+ 10μM Fe2+
Outer membrane
Periplasm
Cytoplasmic membrane
Cytoplasm
MntR/Fur
MntR/yybp-ykoY
MntH
MntP
B
In vitro
Extracellular space
0 μM Mn2+ 0 μM Fe2+
TBDR
MntR/?
TFP
MntR?
MntR/Fur
MntR/yybp-ykoY
MntH
MntP
CDF
RND
C
Amoeba cytoplasm
Fagosomal membrane
Fagosomal Lumen
Bacterial outer membrane
Bacterial periplasm
Bacterial cytoplasmic membrane
Bacterial cytoplasm
Nramp1
ADP + Pi
ATP
NADP+ + H+
NADPH
NOX
TBDR?
MntH
Mn-SOD
Mn-CAT
Reduction of oxidative stress
Interaction
Sm18 - A. castellanii
Interaction
Sm18ΔmntH - A. castellanii
MntH
Increase of oxidative stress
decrease of intracellular replication capacity
Mn2+
Fe2+
Zn2+/Cu2+
Zn2+/Cu2+/Ni2+/Cd2+
Transport direction
Transcription activation
Transcription inactivation